

# Tectonics

## RESEARCH ARTICLE

10.1029/2019TC005533

### Key Points:

- An unknown volcanic-intrusive complex is identified in an area located about 15 km off the Tyrrhenian coast of northern Calabria
- The volcanic edifices formed in correspondence of a shallower crustal volume characterized by low Vp/Vs ratios
- The volcanic-intrusive complex is originated by the decompression melting of mantle material at the northern edge of the Ionian slab

### Correspondence to:

F. Pepe,  
fabrizio.pepe@unipa.it

### Citation:

De Ritis, R., Pepe, F., Orecchio, B., Casalbore, D., Bosman, A., Chiappini, M., et al. (2019). Magmatism along lateral slab edges: Insights from the Diamante-Enotrio-Ovidio volcanic-intrusive complex (Southern Tyrrhenian Sea). *Tectonics*, 38, 2581–2605. <https://doi.org/10.1029/2019TC005533>









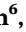



Received 18 FEB 2019

Accepted 30 JUN 2019

Accepted article online 6 JUL 2019

Published online 1 AUG 2019

## Magmatism Along Lateral Slab Edges: Insights From the Diamante-Enotrio-Ovidio Volcanic-Intrusive Complex (Southern Tyrrhenian Sea)

R. De Ritis<sup>1</sup> , F. Pepe<sup>2</sup> , B. Orecchio<sup>3</sup> , D. Casalbore<sup>4,5</sup> , A. Bosman<sup>4</sup> , M. Chiappini<sup>1</sup> , F. Chiocci<sup>5</sup> , M. Corradino<sup>2</sup> , R. Nicolich<sup>6</sup> , E. Martorelli<sup>4</sup> , C. Monaco<sup>7</sup> , D. Presti<sup>3</sup> , and C. Totaro<sup>3</sup>

<sup>1</sup>Istituto Nazionale di Geofisica e Vulcanologia di Roma, Rome, Italy, <sup>2</sup>Dipartimento di Scienze della Terra e del Mare (DiSTeM), Università di Palermo, Palermo, Italy, <sup>3</sup>Dipartimento di Scienze Matematiche e Informatiche, Scienze Fisiche e Scienze della Terra, Università degli Studi di Messina, Messina, Italy, <sup>4</sup>Istituto di Geologia Ambientale e Geoingegneria-Consiglio Nazionale delle Ricerche, Roma, Italy, <sup>5</sup>Dipartimento di Scienze della Terra, Università Sapienza di Roma, Roma, Italy, <sup>6</sup>Via Domenico Rossetti 83, Trieste, Italy, <sup>7</sup>Dipartimento di Scienze Biologiche, Geologiche e Ambientali, University of Catania, Catania, Italy

**Abstract** Volcanic-intrusive complexes often formed along lateral slab edges as a consequence of subduction-induced mantle flow. We investigate this process in the southern Tyrrhenian Sea by integrating multibeam bathymetry, seismic-reflection data, regional magnetic anomalies data, and seismological data. The interpretation of the data highlights the presence of magmatic intrusions that locally reach the seafloor forming volcanic edifices. Chimneys, lava flows, and laccoliths are observed beneath and surrounding the volcanoes. The emplacement and cooling of the magma occurred during the Brunhes Chron. The volcanoes are not active even if the hydrothermal activity occurs. The volcanic-intrusive complex can be subdivided in a western domain (Diamante and Enotrio seamounts) where strike-slip transpressional faults deform the volcanic edifices and an eastern domain (Ovidio volcanic seamounts) characterized by flat-topped volcanic edifices. The flat-topped morphology is the result of the interplay between volcanism, erosion, sedimentation, and sea-level change. The Ovidio volcanic seamounts formed in an area that experienced at least 60 m of subsidence. Magnetic signatures over the northern side of the Ovidio and Diamante seamounts highlight the presence of a deep-rooted, magnetized feeding system remnant. Volcanic edifices extend above a magma feeding system, characterized by low Vp/Vs ratios. The Diamante-Enotrio-Ovidio volcanic-intrusive complex formed as a consequence of the ascent of subduction-induced mantle flow originated in the northern-western edge of the retreating Ionian slab. We speculate that the magma ascent was controlled by a strike-slip deformation belt, which accommodated the bulk of the shear strain resulting from the formation of a roughly E-W trending, Subduction-Transform Edges Propagator fault.

## 1. Introduction

The subduction and retreat of the Adriatic-Ionian plate beneath Eurasia mainly controlled the Tertiary to Recent tectono-stratigraphic evolution of the western Mediterranean Sea. Since the last 35 Ma, the evolution of the subduction zone has been driven by episodes of fast rollback, which caused the opening of the Ligurian-Provençal Basin, and of the Tyrrhenian Sea (Carminati & Doglioni, 2005; Faccenna et al., 2001; Gueguen et al., 1998). According to Goes et al. (2004), in the last 0.5-Ma-related rollback has slowed down to a minor fraction of the 5–6 cm/year average rollback velocities since Tortonian times (Faccenna et al., 2001). In the Tyrrhenian Sea, the extension of the continental lithospheric led to the crustal thinning, mantle exhumation, and development of back-arc basins, the Vavilov (4–2.5 Ma) and the Marsili (1.87–1.67 Ma) basins, floored by oceanic crust (Carminati et al., 2004; Kastens et al., 1988; Prada et al., 2016; Sartori et al., 2004; Figure 1a). Fore-arc basins (Policastro Gulf, Paola Basin, and Gioia Basin) developed along the Tyrrhenian margin of the Calabrian Arc since the late Miocene, as a result of a compressional and strike-slip tectonic regime (Argnani & Trincardi, 1988; Ferranti et al., 2014; Milia et al., 2009; Pepe et al., 2010). The present-day tectonic setting of the Tyrrhenian Basin was achieved about 1–0.7Ma when the plate boundary system reorganized to accommodate the Africa-Eurasia convergence (Goes et al., 2004).

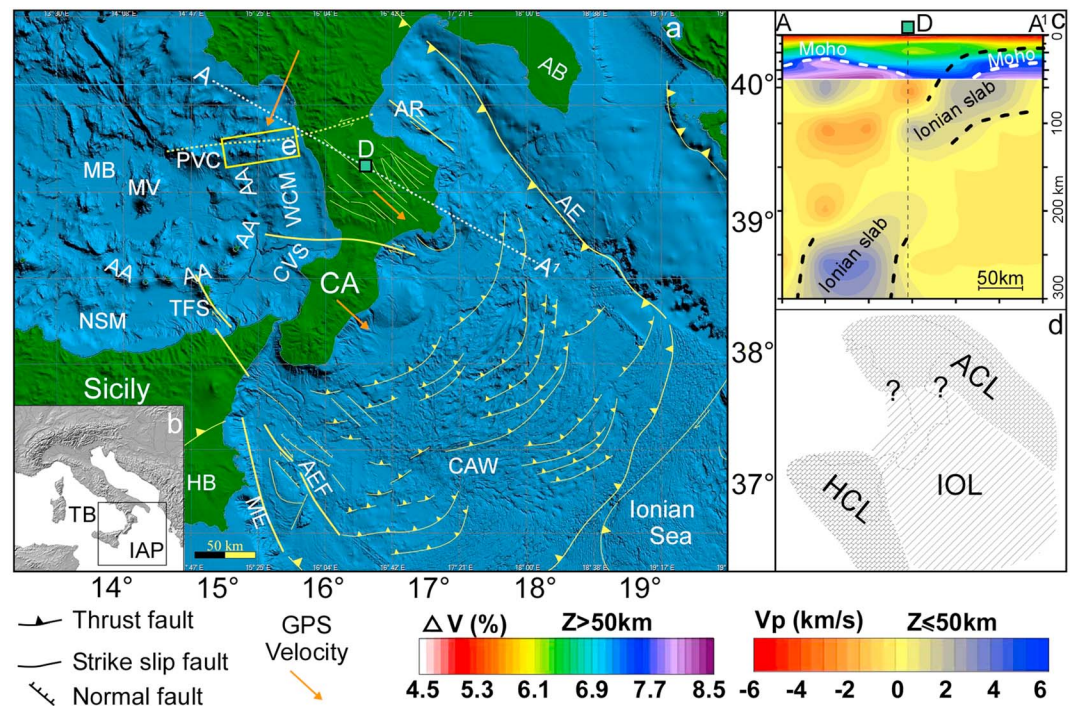


**Figure 1.** (a) Geo-structural sketch map of the study area. Abbreviations: AA, Aeolian Arc; AB, Apulian Block; AE, Apulian escarpment; AEF, Alfeo-Etna Fault; AR, Amendolara Ridge; CA, Calabrian Arc; CAW, Calabrian accretionary wedge; CVS, Capo Vaticano promontory; HB, Hyblean block; ME, Malta escarpment; MB, Marsili basin; MV, Marsili Volcano; NSM, northern Sicilian margin; PVC, Palinuro volcano chain; TFS, Tindari Fault System; WCM, western Calabrian margin. The AA' dotted line is the track of the profile shown in panel c. (b) Location of the area shown in the box a. Abbreviations: IAP, Ionian abyssal plain; TB, Tyrrhenian basin. (c)  $P$  wave velocity section obtained by the tomographic model (Neri et al., 2009). (d) Sketch map of the lower plates of the Central Mediterranean subduction system. Abbreviations: IOL, Ionian Oceanic Lithosphere, ACL, Adriatic Continental Lithosphere, HCL, Hyblean Continental Lithosphere. (e) Study area including the Diamante, Enotrio, Ovidio, and Scalea seamounts.

Tearing and segmentation of subducting oceanic lithosphere are common processes in subduction systems (Carminati et al., 1998; Chatelain et al., 1992; Lallemand et al., 2001; Levin et al., 2002; Miller et al., 2006; Wortel & Spakman, 2000). These processes can be consequent to (i) changes in the velocity of subduction rollback (Govers & Wortel, 2005), (ii) the lateral variation of nature (continental or oceanic) or thickness of the slab (Argnani, 2009), and (iii) local collisional events (Sacks & Secor, 1990). At slab edges, Subduction-Transform Edge Propagator (STEP, also called tear) faults occur (Govers & Wortel, 2005). STEP faults produce tearing in the slab and generally propagate perpendicular to the subduction strike (Nijholt & Govers, 2015). Most of them show vertical motion between the two blocks of the underthrusting plate at both sides of the STEP fault and normal to strike-slip movements in the upper plate (Baes et al., 2011; Govers & Wortel, 2005).

The coupling of subducting slab with viscous mantle can generate three-dimensional, time-dependent mantle circulation characterized by poloidal and toroidal circulation components (Funicello et al., 2006; Király et al., 2017; Liu & Stegman, 2012; Strak & Schellart, 2014). The subduction-induced mantle flow produces a mantle upwelling located laterally to the slab edges (Strak & Schellart, 2014). Faccenna et al. (2010) and Strak and Schellart (2014) also suggest that the upwelling mantle flow can trigger slab tear-related magmatism during fault propagation, responsible for off-arc volcanism in laterally confined subduction zones. This process can explain the formation of localized and aligned magmatism developed along tear faults of the Ionian slab (Gasparon et al., 2009; Rosenbaum et al., 2008).

Magmatism associated with the decompression melting of upper mantle material that flows along a lateral slab edge is insufficiently documented in the Tyrrhenian-Ionian subduction system. In particular, the intra-plate volcanism that occurs in linear chains close to the lateral Ionian slab edges is partly defined and its origin and evolution poorly understood. Recently, Cocchi et al. (2017) report the presence of several volcanoes,

forming the ~90-km-long submarine Palinuro volcanic chain (hereafter PVC; Figure 1a) above the northern boundary of the Ionian slab. Although the authors documented one of the largest volcanic activity zones of the Southern Tyrrhenian Sea, a complete overview of the magmatism located along this STEP fault needs more accurate analyses and inspection.

Magmatic activity accompanied the retreat of the Adriatic-Ionian plate. Since the late Miocene, magmatic activity occurred near the coasts of Sardinia producing volcanic seamounts and arc-shaped magmatic fronts and became progressively younger eastward and southeastward (Argnani & Savelli, 1999; Locardi, 1993; Peccerillo, 2017; Savelli, 1988, 2015). In this work, we investigate a poorly documented large volcanic-intrusive complex developed in shallow water up to 1,000-m water depth, east of the PVC in the northern offshore of the Calabrian Arc (NOCA) during the Pleistocene. The volcanic-intrusive complex comprises the Diamante, Enotrio and Ovidio seamounts (hereafter DEOSs; Würtz & Rovere, 2015) and extends 50 × 40 km in the NS and EW directions, respectively (box e in Figure 1a).

Data and interpretation here presented, integrated with those available in the literature, will depict a case study and give constraints to understand the origin and evolution of the volcanic-intrusive complex formed over a STEP fault because of subduction-induced mantle flow.

## 2. Geological Setting

The Tyrrhenian Sea is a Neogene to Recent basin developed in the upper plate of the Tyrrhenian-Ionian subduction system within the frame of Eurasia-Africa convergence. The seismic tomography data highlight that the lower plate is not continuous and lithospheric segments are separated by STEP faults (Lucente et al., 1999; Piromallo & Morelli, 2003; Wortel & Spakman, 2000). In particular, tomographic cross sections show the presence of orogen-perpendicular lithospheric-scale structures that accommodated strike-slip displacements during slab tearing propagation (Rosenbaum et al., 2008, and references therein).

Beneath the Calabrian Arc, the lower plate of the Tyrrhenian-Ionian subduction system is represented by the Ionian slab dipping ~70° to 80° northwestward (Chiarabba et al., 2008; Neri et al., 2009; Orecchio et al., 2014; Piromallo & Morelli, 2003; Scarfi & Barberi, 2018; Wortel & Spakman, 2000; Figure 1c). Catalano and Sulli (2006), de Voogd et al. (1992), and Finetti and Del Ben (1986) suggested an “oceanic” nature of the Ionian plate. Alternatively, Boccaletti et al. (1984), Cernobori et al. (1996), Ismail-Zadeh et al. (1998), Locardi and Nicolich (2005), and Panza et al. (2003) hypothesized that the lower plate consists of a thinned continental crust about 6-km thick in the center but thickening to 9 km at the western margin toward the Malta Escarpment. Recently, Dannowski et al. (2018) and Dellong et al. (2018) documented the oceanic nature of the Ionian Abyssal Plain, based on crustal thickness (6 km in the center and 9 km at the western margin) and seismic velocities compatible with oceanic crust. The wide Ionian basin appears confined between two main physiographic features, the Malta escarpment (Figure 1a) to the southwest and the Apulia escarpment to the northeast. Unstretched continental crust, corresponding to the prolongation of the subducted continental crust beneath the Southern Apennine and Sicilian fold and thrust belt, is inferred both in the Apulian and Hyblean blocks, respectively (Catalano & Sulli, 2006, and references therein; Figures 1a and 1d).

The upper plate of the Tyrrhenian-Ionian subduction system includes the back-arc domain of the SE Tyrrhenian Sea (Marsili Basin in Figure 1a), volcanic seamounts along arc-shaped structure (AA in Figure 1a), the fore-arc region including the Calabrian-Peloritan Arc, and farther to the southeast the Calabrian accretionary wedge (Figure 1a). The Marsili Basin represents the youngest back-arc oceanic basin formed on the overriding plate of the subduction system during the Pleistocene (Kastens et al., 1988; Nicolosi et al., 2006). An NNE-SSW elongated volcanic ridge (Marsili Volcano in Figure 1a) developed at the center of the Marsili Abyssal Plain during the last 0.78 Ma (Marani & Trua, 2002).

The ring-shaped Aeolian arc (AA, in Figure 1a) developed in the northern Sicilian margin and western Calabrian margin during the Quaternary (Beccaluva et al., 1985; Gillot, 1987; Santo & Clark, 1994, Figure 1a). The calc-alkaline to shoshonitic and k-alkaline affinity of their volcanic products is related to the subduction of the Ionian slab beneath the Calabrian Arc region (Barberi et al., 1973; Beccaluva et al., 1985; Chiarabba et al., 2008; Ferrari & Manetti, 1993). Aeolian volcanism is characterized by a relationship between upper crustal structures along the upper plate of the Tyrrhenian-Ionian subduction

system and structural/volcanic sectors characterized by different regional stress fields (De Astis et al., 2003, and reference therein). Recently, Cocchi et al. (2017) document a ~90-km-long submarine volcanic belt (PVC in Figure 1a). The PVC is composed by arc-type central volcanoes and fissural, spreading-type centers emplaced along second-order shears of a left-lateral strike-slip fault. Overall, the volume of the investigated volcanic belt is larger than that of the island-arc edifices and the Marsili Volcano. Cocchi et al. (2017) also suggest that such a large volume of magma is originated by an upwelling of the isotherms due to mantle melts upraising from the edge of the slab along a STEP fault. The lithospheric-scale structure was inferred farther to the East, along the transition zone between the Calabrian Arc and the Southern Apennines, at depth less than 100 km (Rosenbaum et al., 2008), based on positive  $P$  wave seismic anomalies (Lucente et al., 1999).

A tomographic analysis showed Mt. Etna volcano lying on the top of an upper mantle low-velocity anomaly at the southern edge of the Ionian slab (Barreca et al., 2018; Montuori et al., 2007). Faccenna et al. (2010) propose this volcano is the result of complex 3-D mantle circulation caused by subducting lithosphere at the southern side of the Ionian slab. Geochemical evidence (Trua et al., 2003) and the seismic anisotropy (Baccheschi et al., 2007; Civello & Margheriti, 2004) also suggest the presence of a toroidal mantle flow around the Ionian slab. Faccenna et al. (2010) show other inactive volcanoes located inside the Mediterranean at the edges of the slab and interpret these structures as off-volcanic-arc-volcanism generated by the decompression melting produced by 3-D slab induced mantle circulation. The occurrence of Pleistocene intrusive and off-arc volcanic activities is also documented in the area between the Aeolian back arc volcanoes and the Capo Vaticano promontory (De Ritis et al., 2010; Loreto et al., 2015, CVS in Figure 1a). Here the uprising of magma was favored by Pliocene NW- and Pleistocene NE-trending normal faults systems. Both fault systems account for the high level of fracturing.

### 3. Materials and Methods

This study is based on the integration of different geophysical data: (a) multibeam sonar bathymetry, (b) high-penetration multichannel seismic-reflection data, (c) magnetometric data, and (d) seismological data.

Multibeam bathymetry allowed depicting the morphology of the seafloor with unprecedented detail, especially in shallow water sectors. At greater depths, the decrease in resolution hinders the recognition of small-scale volcanic/tectonic/erosive-depositional geomorphic features. Moreover, a geomorphic feature could be the result of different or multiple geological processes acting on the seafloor and subseafloor. Thus, its correct interpretation required the integration with other marine geophysical techniques (e.g., seismic and magnetic anomaly).

Seismic reflection data set allowed the identification of volcanic-intrusive complexes within and above the sedimentary succession. The sequence-stratigraphic analysis allowed the identification of a geomorphological indicator of vertical movements, helpful to estimate the subsidence of a volcano. However, it is essential to note that seismic data must be integrated with regional magnetic anomalies and multibeam bathymetry data to confirm the volcanic origin of the edifices and to obtain a map view of the fault lineaments, respectively.

Magnetometric data highlighted the volcanic nature of the DEOS and suggested the existence of a deep-rooted volcanic complex. However, potential field data have an intrinsic ambiguity, since an anomaly can be reproduced by an infinite number of sources distributions. Thus, the modeling obtained from the analysis of magnetometric data must be supported by other geophysical data.

Local earthquake tomography provided a 3-D model of  $V_p$  and  $V_p/V_s$  up to 27 km of depth, useful to obtain a view of the local structure at deeper depths the overall investigation of the DEOS system. In spite of a lower degree of resolution with respect to the other methodologies, the tomography has allowed to extend in depth the overall investigation of the DEOS system.

#### 3.1. Multibeam Sonar Data

A digital elevation model (DEM) with a cell size of 20 m was produced by an integration of different high-resolution multibeam bathymetry data set (Figure 2). The morpho-bathymetric survey was carried out between 2009 and 2011, aboard the *R/V Urania*, *Maria Grazia* and *Minerva 1* (Research vessel of the National Research Council), using a Kongsberg EM710, EM3002D multibeam equipment for shallow



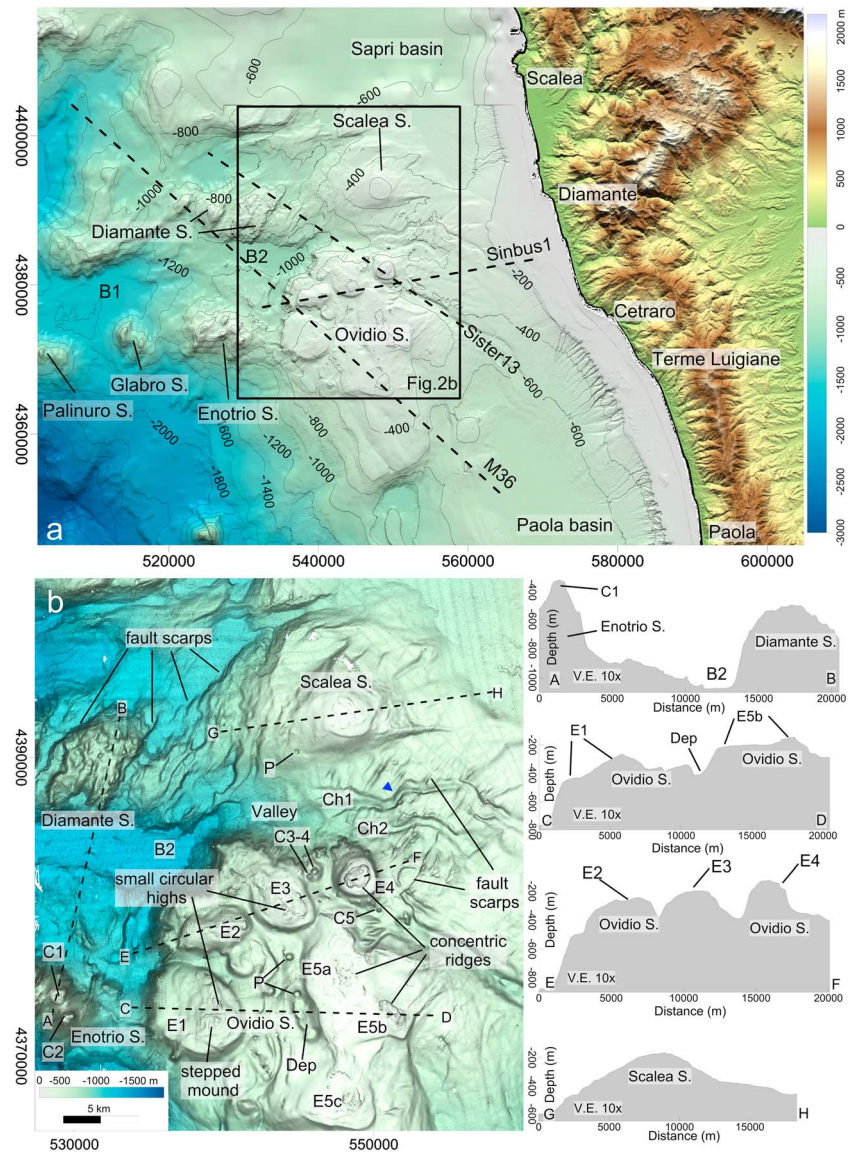


**Figure 2.** (a) Digital Elevation Model (DEM) of the Western Calabrian Offshore area including the southern and the northern parts of the Sapri and Paola basins, respectively, the eastern portion of the Palinuro Glabro seamounts chain and the Enotrio, Ovidio, Diamante, and Scalea seamounts. This DEM derives by merging the EMODnet lower resolution bathymetric data to the high-resolution multibeam data collected during the MaGIC project; B: basin; S: Seamount. (b) High-resolution DEM of the study area (for location black box in Figure 2a). In the right panel are reported the bathymetric profiles crossing the main volcanic edifices (dash lines in the left panel). E1-5: flat-topped volcanic edifices forming the Ovidio Seamount; C1-5: small volcanic cones; P: pockmark; Dep: depression; Ch: channel; B: basin.

water and Teledyne Reson 7160, for deep water operating at frequencies from 44 to 300 kHz. A differential GPS provided data positioning; sound velocity profiles of the water column were daily collected. Moreover, patch test lines were conducted during each research survey to minimize errors due to the orientation of the transducers. Data were processed by using the Caris Hips and Sips 8.1 software through the application of statistical filter and manual editing. The soundings data were corrected through sound speed profiles and local tide.

The high-resolution multibeam bathymetry was integrated with a DEM with cell size of 250 m derived by EMODnet-Bathymetry portal (EMODnet Bathymetry; <http://doi.org/10.12770/c7b53704-999d-4721-b1a3-04ec60c87238>) both for the deeper portions (water depths greater than 900 m) and the northernmost area (Figure 2a).

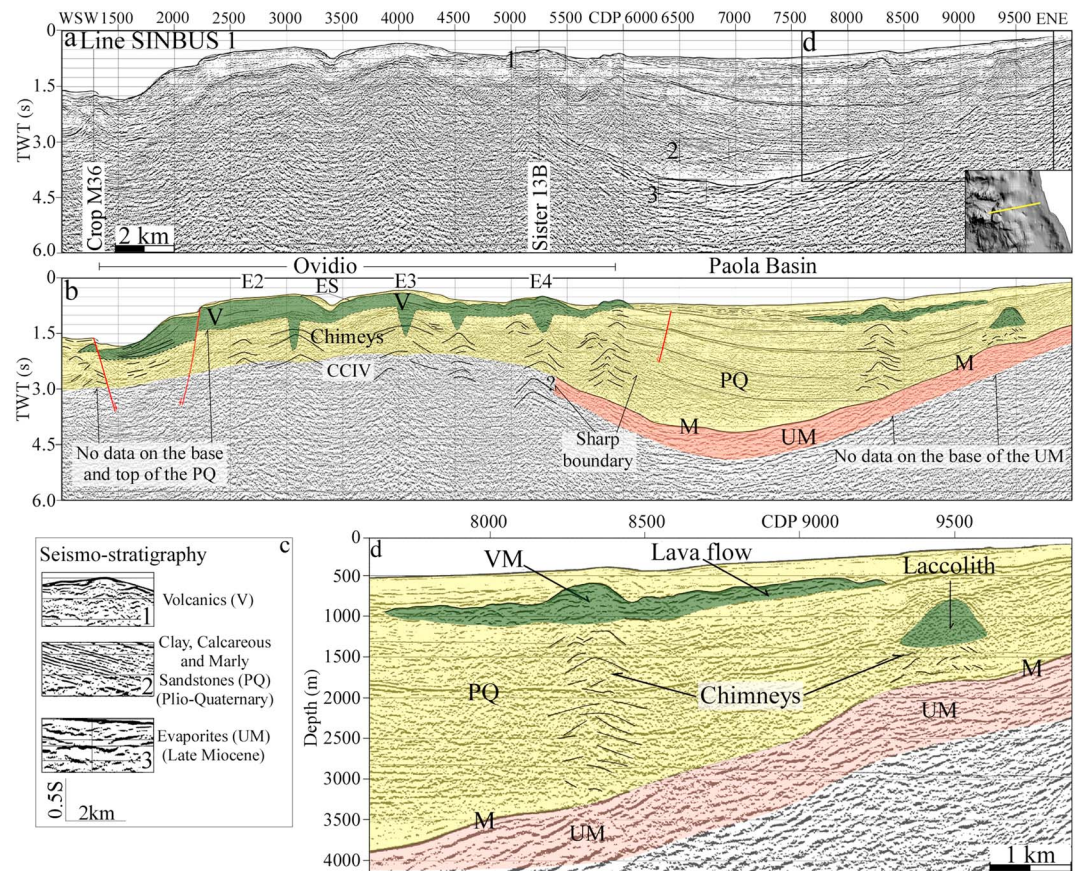


**Figure 3.** (a) Seismic line SINBUS 1 and (b) its interpretation. Inset shows the location of the profile (see also Figure 2a). (c) Seismic stratigraphy units recognized on seismic profiles; (d) Zoom of the right part of the (depth converted) seismic line SINBUS 1. Abbreviations: ES, erosional surface; M, Messinian horizon; PQ, Plio-quaternary deposits; UM, Upper Miocene deposits; V, volcanics; VM, volcanic mound.

### 3.2. High-Penetration Seismic Reflection Data

Three seismic lines were used for this study (see location in Figure 2a). The high-penetration, multichannel seismic line Sinbus 1 crosses the investigated area in almost E-W direction (Figure 3). This profile is part of the seismic reflection data set recorded by the Osservatorio Geofisico Sperimentale of Trieste (Italy) with the DINMA–University of Trieste and IGP–Paris, in the frame of the SINBUS project. A 3,600-m streamer long with 144 active channels recorded signals generated by a standard tuned air guns array totaling 60 L. A shooting interval of 25 m allowed a 6,000% coverage with 8-s recording length and 2-ms sampling interval. Prestack processing of data operated with the following sequences: amplitude recovery and signature conversion to minimum phase, spike deconvolution, velocity analysis every 1.5 km, normal move out correction, mute and sixtyfold stack and wavelet shaping to zero phase. Poststack processing utilized an FK filter, wave equation migration, time-variant filter, and dynamic trace equalization.

The regional high-penetration, multichannel seismic line CROP M36, acquired in the frame of the CROP-Mare project in 1994 (Finetti, 2005; Scrocca et al., 2003), is oriented NW-SE (Figure 4). A 4,500-m streamer long with 180 active channels recorded signals generated by an air gun array of 4,906 cubic inches. A shooting interval of 50 m allowed a 4,500% coverage with 17-s recording length and 4-ms sampling interval. The adopted processing sequence included the application of the following routines: antialiasing filter and resampling, geometry definition, amplitude recovery, deconvolution, preliminary velocity analysis, multiple attenuation in the F-K domain, velocity analysis, normal move out and stack, time-variant filters, and marine statics.

The multichannel seismic line Sister 13B extends in NW-SE direction (Figure 5). This profile is included in the seismic data set recorded by the CNR Geomare Sud Napoli (Italy) with the Vrije Universiteit Amsterdam



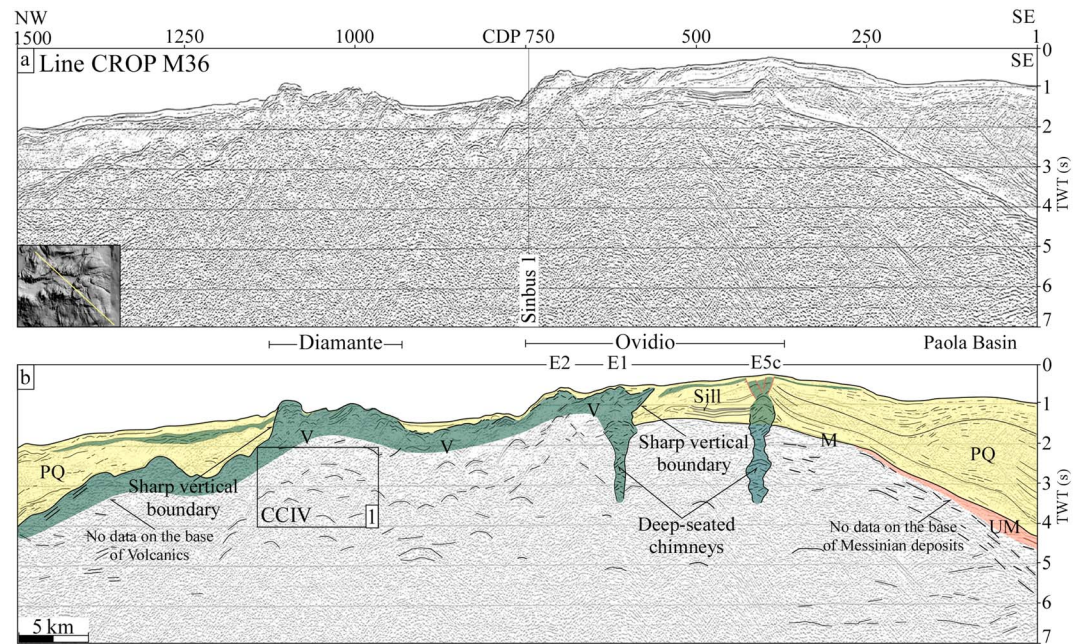


**Figure 4.** (a) Seismic line CROP M36 and (b) its interpretation. Inset shows the location of the profile (see also Figure 2a). Abbreviations: M, Messinian horizon; PQ, Plio-quaternary deposits; V, volcanics; UM, Upper Miocene deposits. Box 1 shows magmatic intrusions into the continental crust (unit CCIV).

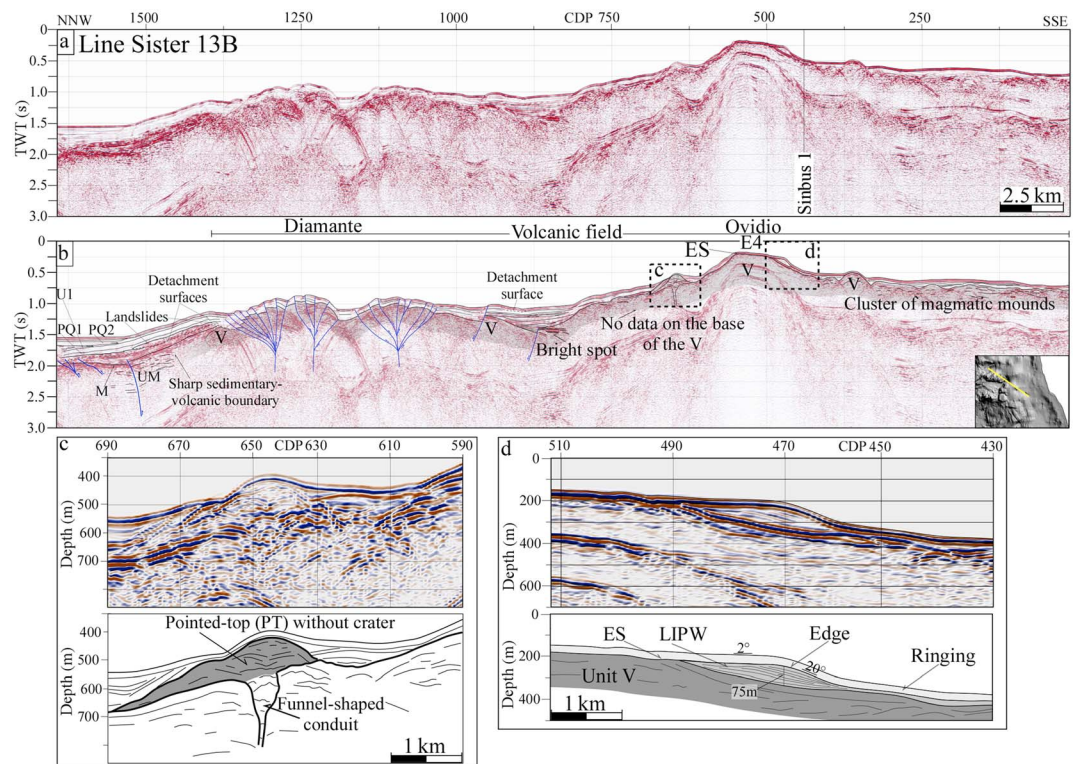


**Figure 5.** (a) Seismic line Sister 13B and (b) its interpretation. Inset shows the location of the profile (see also Figure 2a). (c and d) Zoom of the depth-converted parts of the seismic line Sister 13B (for location see boxes c and f in Figure 5b). Abbreviations: ES, erosional surface; LIPW, Lowstand Infralittoral Prograding Wedge; M, Messinian horizon; PQ, Plio-quaternary deposits; V, volcanics; UM, Upper Miocene deposits.

and the Marine Geology Group of the University of Palermo, in the frame of the SISTER99 project in 1999 (Pepe et al., 2010). A 300-m streamer long with 12 active channels recorded signals generated by a 75-cubic inch air gun. A shooting interval of 25 m allowed a 600% coverage with 7-s recording length and 1-ms sampling interval. Prestack data processing includes amplitude recovery, spherical divergence correction, deconvolution, velocity analysis every 50 CDP, normal move out, and stack. The poststack processing continued with surface related multiple attenuation, mixing of three traces to enhance horizontal signals, band-pass “finite impulse response” time-variant filters, time variant gain to boost amplitudes of deeper arrivals.

The seismic and sequence-stratigraphic analysis allowed the reconstruction of the depositional architecture of stratigraphic units as well as the identification of magmatic intrusions. Following the analysis of acoustic facies, the thickness of sediment and volcanic deposits were derived from time to depth conversion of the seismic lines, using velocities of 1,500 and 2,100 m/s for the water column and the Plio-Quaternary deposits, respectively. The value of 2,100 m/s matches velocity profiles and sonic log data available for coeval deposits in wells drilled in similar offshore settings (see Pepe et al., 2010 for details).

### 3.3. Magnetic Data Set and Modeling

The most recent regional magnetic anomaly map for the Italian region (Figure 6a) is described in Caratori Tontini et al. (2004). This field is derived from airborne surveys carried out by AGIP between 1971 and 1980. The surveys were flown at 1,460 m, along NE-SW and NW-SE oriented profiles on the whole country. The data set was compiled using 36 original micro surveys executed by the company and published in the first magnetic anomaly map of Italy (Agip, 1981). Calabria flight lines were collected in 1973 and are mostly SW-NE oriented, 5-km spaced apart whereas tie lines cross orthogonally with a distance of 10–15 km. The external geomagnetic variations were removed using the base stations placed at the center of each survey during the time of flights. The revised anomaly map of Caratori Tontini et al. (2004) was recalculated using a different appropriate reference field (IGRF) and corrected for each area and time of measurements. Therefore, we digitalized the Caratori Tontini et al. (2004) field inside a window encompassing as better as possible the area of interest (Figure 6a) based on its contouring and color scale (Lawrence et al., 1996). The obtained digital data have been compared with the shipborne regional field, published in Chiappini (2000), reduced at the same epoch and projected at the same altitude (upper continued, Blakely, 1996) of the Caratori Tontini et al. (2004) field. The obtained smoother field (less noisy), despite the regional character, was profitably used to obtain a qualitative and quantitative characterization of the magnetic anomaly field (hereafter total magnetic intensity, TMI) of the investigated area (Figure 6b). The TMI shows a magnetic singularity (anomaly A in Figure 6b) in the almost not magnetic NOCA (excluding the highly magnetized PVC; Cocchi et al., 2017).

The dipolar nature of the TMI field makes its interpretation difficult, especially where the effects of adjacent sources overlap. The reduction-to-the-pole transformation (hereafter RTP-TMI) removes this difficulty, transforming each dipolar anomaly into a positive or negative anomaly and shifting it to the vertical of its source (Baranov & Naudy, 1964; Blakely, 1996). To carry out the RTP transformation, we used the Earth's magnetic field angular values derived by the IGRF model (IGRF-1978; <http://www.noaa.gov>) computed for the time of the measurements (Figure 6c).

The study area is characterized by low values of the magnetic anomaly field ( $-10 < nT < 20$ ) and, by several high intensity, single and composite dipoles (Figures 6a and 6c). These values suggest the presence of a continental crust characterized by low magnetic properties and highly magnetized sources, usually in correspondence of volcanic seamounts. Moreover, a percentage of feeding magmas does not reach the surface and crystallize at deep and shallower depths, forming magmatic intrusions. These often create a noteworthy magnetization contrast with respect to the surrounding hosting rocks. As a consequence, the magnetic maps allow revealing the presence of magmatic intrusions, whereas magnetic modeling provides information about their geometry and depth.

In this work, we used 3-D voxel inversion code MGinv3D ([www.scicomap.com](http://www.scicomap.com)) for an unconstrained modeling (without initial or reference model) of the TMI data shown in Figure 6d. The subsurface below the anomaly A was discretized by cubic cells  $500 \times 500 \times 400$  m in the easting, northing and depth directions, respectively. We used padding cells to expand the total volume, with a maximum mesh depth of 6 km below sea level (hereafter bsl) and with a total mesh count of 116 (E–W) by 124 (N–S) and 29 (depth). The algorithm



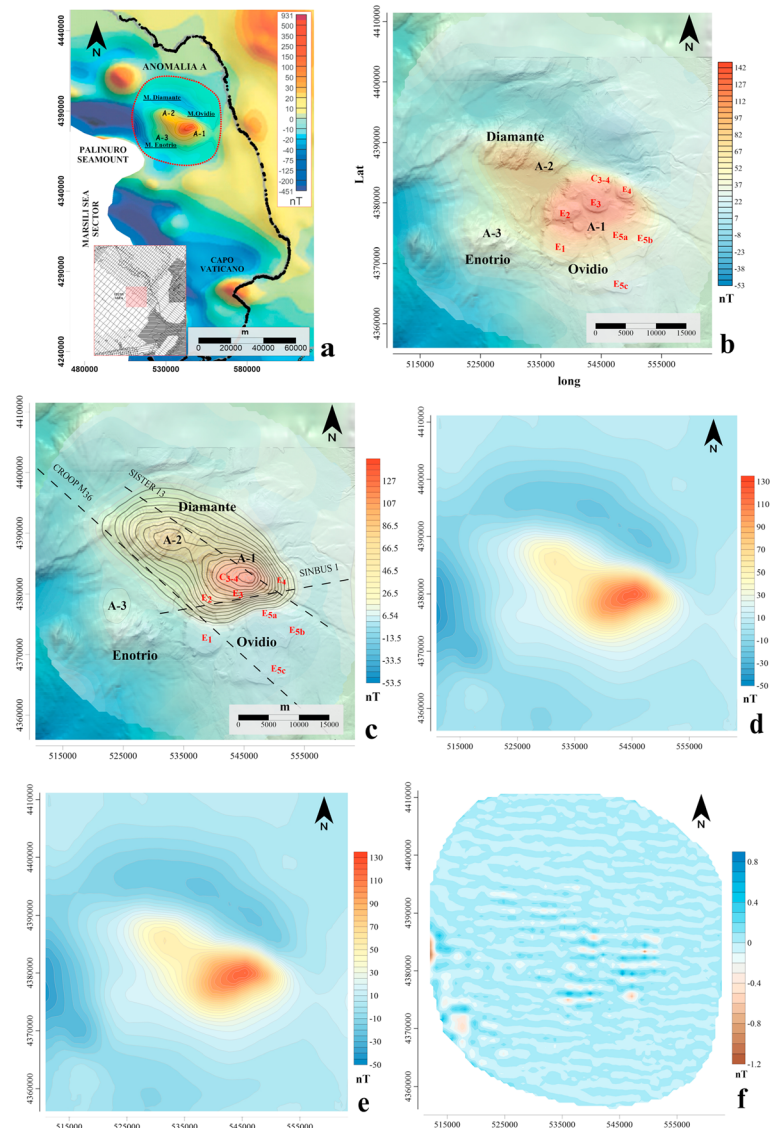


**Figure 6.** Regional magnetic anomaly field of the western Calabrian offshore (Caratori Tontini et al., 2004) and its acquisition grid in the left bottom panel. The red circle circumscribes the magnetic anomaly-A modeled and interpreted in the paper (a); digitalized and corrected magnetic A-anomaly (TMI) along with its subanomalies subdivision (b); reduced-to-the-pole magnetic anomaly-A together with the seismic profile tracks (c); observed magnetic anomaly data sampled in the original data set at the mesh cell center and used in the inverse modelling (d); magnetic anomaly data predicted by the model (e); and inversion error (misfit) expressed as difference between the observed and predicted magnetic anomaly data (f).

uses an approach similar to the smooth inversion technique described by Li and Oldenburg (2003). The difference is that the modeling volume used in this study is composed of prismatic cells draped underneath the topography rather than simple rectangular prisms. The TMI grid was sampled at the mesh cell center for a total of 27,947 data points. Using unit smoothness weights in the  $x$ ,  $y$ , and  $z$  directions, the data were fit to rms data misfit of 20 nT after 300 iterations. Inverse modeling results, together with the observed and predicted fields, are shown in Figures 6d–6e and 7.

### 3.4. Seismic Data for Local Earthquake Tomography

Local earthquake tomography of the NOCA sector was carried out using seismic data collected from the national network of the Istituto Nazionale di Geofisica e Vulcanologia, the local networks operating in Calabria and Sicily (Orecchio et al., 2011) and the LOTOS inversion algorithm (Koulakov, 2009). The 3-D

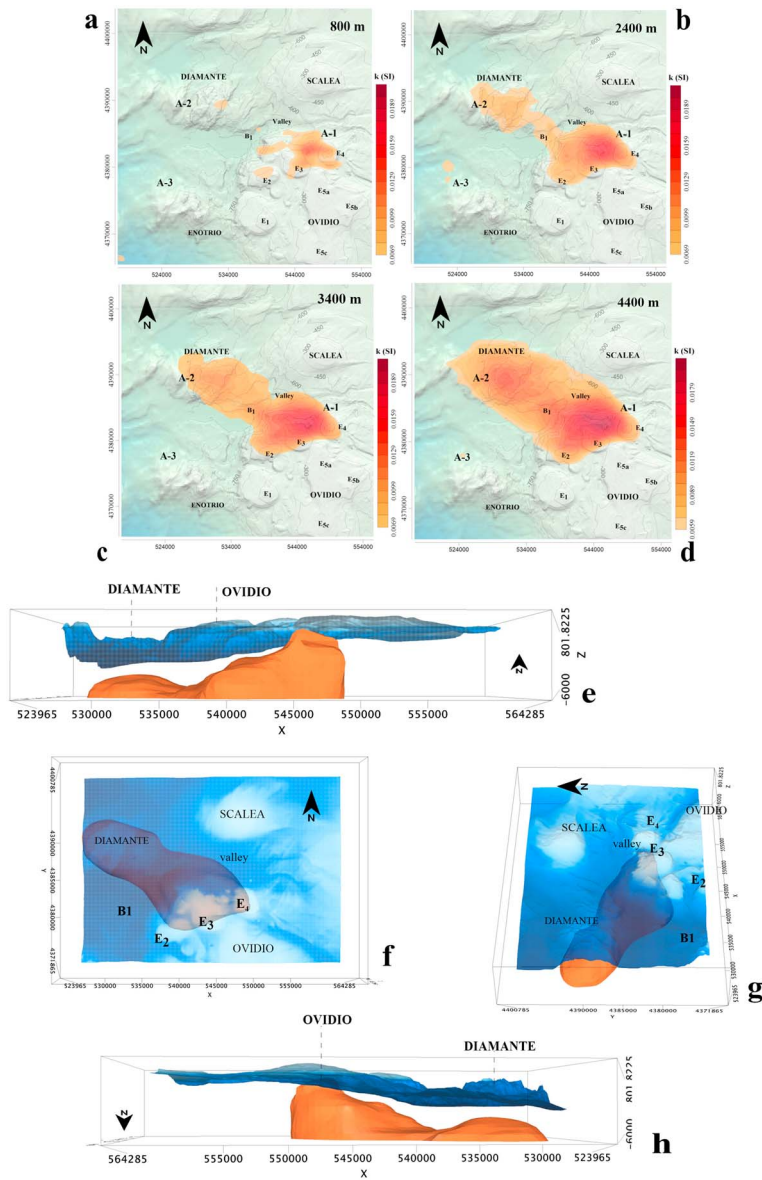


**Figure 7.** Inverse model shown as color scaled  $xy$  slices at different depths (a–d), overlapping the contouring and shaded relief Digital Elevation Model of the study area. The 3-D inverse model represented by the 0.01 SI susceptibility iso-surface (orange) encompassing most of the rock volume with meaningful magnetic properties below the Digital Elevation Model (blue color scale): (e) southern point of view, (f) 3-D azimuthal view, (g) eastern point of view; and (h) northern point of view.

seismic velocity structure of the DEOS area was properly recovered inverting the data in a wider sector. This choice allowed to get a denser ray coverage as well as a higher resolution. We selected earthquakes occurred between 1985 and 2014 and located at depth shallower than 100 km in the Calabrian Arc region. A quality selection has been applied following two criteria: The total number of P and S picks per event should be larger or equal eight and the residuals of P and S data, after location in the 1-D starting model, should be smaller than 1.5 and 2 s, respectively. The final data set used for tomographic inversion consisted of 9,295 earthquakes and corresponding 85,704 P and 50,300 S arrival times coming from about 531 stations. By using the LOTOS code (Koulakov, 2009), the calculations start with preliminary source locations based on the grid search method using travel times computed in a 1-D starting velocity model. We estimated the optimal 1-D velocity distribution by repeating the location procedure with several different 1-D models and by selecting the one providing the maximum number of events and picks and minimum average

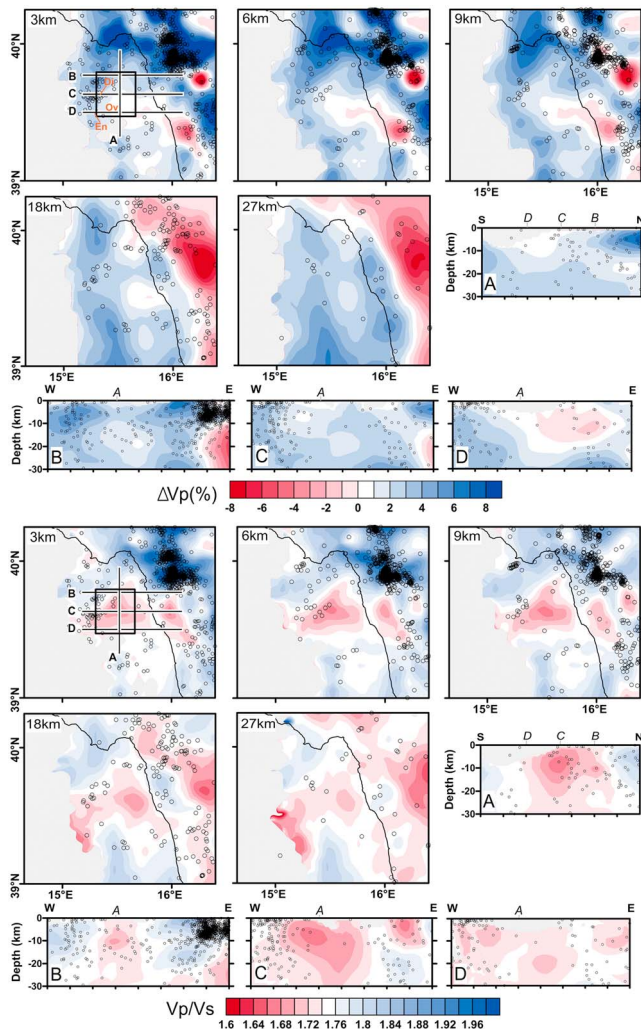


**Figure 8.** Tomographic results reported in terms of percentage variations of  $P$  wave velocity with respect to the starting 1-D model ( $\Delta V_p$ ; top) and  $V_p/V_s$  ratio (bottom). Plates corresponding to 3-, 6-, 9-, 18-, and 27-km depth and four vertical sections A, B, C, and D (see profiles in the 3-km depth plates) cutting the sector of primary interest of this study are shown both for  $\Delta V_p$  and  $V_p/V_s$ . Black circles indicate the distribution of relocated events lying within  $\pm 1.5$  km of the horizontal plates and  $\pm 2.5$  km of the vertical sections. Di, En, and Ov in the top-left map stand for Diamante, Enotrio, and Ovidio, respectively.

deviations of residuals. Source locations in the 3-D velocity model use 3-D ray tracer based on the bending method, which ensures fast, stable calculations of travel times of seismic rays between any two points in the study volume. The velocity distribution is parameterized with a set of nodes distributed in the study area according to ray density. In map view, the nodes are located on a regular grid (spacing of 5 km in our case). In the vertical section, the grid spacing depends on data density, but it cannot be smaller than a predefined value (3 km in our case). To avoid any bias related to the basic orientation of the grid, we performed the inversions for several grids with different basic orientations ( $0^\circ$ ,  $22^\circ$ ,  $45^\circ$ , and  $67^\circ$  in our case). The results computed for these grids are averaged in a regular mesh, used successively as an updated 3-D velocity model for the next iteration. The inversion runs simultaneously for  $P$  and  $S$  velocity distributions, source corrections, and station corrections. The inversion of the matrix is performed using the algorithm for Sparse Linear Equations and Sparse Least Squares (LSQR algorithm, Nolet, 1987; Paige & Saunders, 1982). We regularize the solution by minimizing the gradient between neighboring nodes. The value of smoothing coefficients is estimated based on the results of synthetic modeling.

To evaluate the real accuracy and resolution of the tomographic model, we have performed several synthetic tests (e.g., Foulger et al., 2013; Totaro et al., 2014, 2015), attesting that the velocity structure is satisfactorily recovered in most of the inverted area. Therefore, we demonstrated the inversion parameters are adequate to provide good quality reconstructions.

The final 3-D velocity model has been obtained after five iterations of the tomographic inversion, and it has furnished a reduction of the residual average deviations for  $P$  and  $S$  data of  $\sim 17\%$  and  $\sim 31\%$ , respectively (Figure 8). Even if the study area only includes the Diamante, Enotrio, and Ovidio seamounts, we report for completeness the results of the local earthquake tomography in the whole inverted area.

## 4. Results and Interpretations

### 4.1. Northwestern Calabrian Offshore Seafloor Morphology

The study area corresponds to the intra-slope ridges separating the Sapri and Paola basins (Figure 2a). The bathymetry ranges from 120 to 3,000 m (i.e., from the shelf break down to the easternmost part of the Marsili bathyal plain) and is characterized by a complex morphology due to the occurrence of seamounts, volcanic cones, fault scarps, ponded basins, channelized features (canyons and gullies), and pockmarks. The seamounts form two chains (Figure 2a): The southern chain is formed by the E-W alignment of Palinuro, Glabro, Enotrio, and Ovidio seamounts, whereas the northern chain is mainly formed by Diamante and an easternmost, unknown seamount (hereafter named the Scalea seamount in Figure 2a).

*Enotrio* is an ENE–WSW elongated seamount, with a size of  $10 \times 7$  km and height of  $\sim 500$  m with respect to the surrounding seafloor (Figure 2b). Its western part is characterized by a series of ridges and elongated cones aligned between  $N15^\circ$  and  $N32^\circ$  directions. The eastern part of the seamount exhibits two small cones (named C1 and C2 in Figure 2b; see also the bathymetric sections A–B) marked by flat-topped summits at depths of  $\sim 320$  and 250 m, respectively.

*Ovidio* seamounts mainly consist of five flat-topped morphological highs (named E1–E5 in Figure 2b), covering an area of  $\sim 300$  km<sup>2</sup>. E1 has a subrounded shape, with a size of  $6.7 \times 5$  km and height of a few hundreds of meters. The upper part of the edifice is quite flat and slightly asymmetric, with a shallower and rugged south-eastern side, gently sloping (less than  $5^\circ$ ) toward the deeper and smoother northwestern side (C–D in



Figure 2b). The outer edge of the flat-topped surface lies at depths ranging between 300 (SE) and 500 m (NW). E2 shows an elliptical shape, with a size of  $5 \times 2.7$  km and a height of 150–200 m (E–F in Figure 2b). E2 is a flat-topped edifice, with the outer edge located at depths of 300–350 m, except for a narrow and WSW-ESE elongated ridge present at the summit. E3 has a subrounded shape, with a size of  $4.6 \times 3.8$  km and heights of 150–170 m. E3 is generally flat topped and smooth, with the outer edge located at depths of 220–260 m (E–F in Figure 2b). The central part of E3 shows a rough morphology due to the occurrence of small (up to 10-m high) rocky outcrops. E4 also displays a subrounded shape, with an average diameter of 2.5 km and has heights of 220–300 m. It is a flat-topped and smooth edifice, with the outer edge located at depths ranging between 200 and 250 m (profile E–F in Figure 2b). The central part of E4 is characterized by a subcircular and 20-m-high rocky outcrops. Smaller cones are also observable to NW and SE of E4 (C3–C5 in Figure 2b). As a whole, E2, E3, and E4 edifices are roughly aligned along a WSW-ESE direction. Differently, from the previous edifices, E5 shows an irregular shape, extending over an area of  $75 \text{ km}^2$  and has an overall height of 150–200 m. This irregular shape can be related to the coalescence of three smaller flat-topped highs located in the northwestern, eastern, and southern side (E5a, E5b, and E5c, respectively, in Figure 2b). The morphological trace of these highs is roughly outlined by the elliptical plan-view shape of their outer edge (ranging at depths of 200–250 m) as well as by the occurrence of small and 10- to 30-m-high rocky outcrops in these areas. Noteworthy, a series of enclosed bathymetric lows and subcircular pockmarks (Dep and P in Figure 2b) are aligned in the SSE-NNW direction along the western flank of E5 (bathymetric sections C–D in Figure 2b). Pockmarks have an average diameter of 500 m and relief of 30–50 m.

*Diamante* seamount, located to the northwest of Ovidio, has a size of  $13 \times 7$  km and heights of 250–300 m (Figure 2a). Its southern side is higher (about 560 m) because it lies above a steep, 200-m-high fault scarp bordering the basin B2 (A–B in Figure 2b). *Diamante* seamount can be morphologically divided into two sectors: The western sector is made up of two elliptical volcanic edifices elongated along an SW-NE direction (Figure 2a). The eastern sector shows a peculiar morphology defined by two main morphological highs pervasively affected by a network of steep and linear scarps oriented between  $N10$  and  $N34^\circ E$  (Figure 2b). These scarps have heights ranging from several meters up to 170 m and lengths of 1–6 km.

*Scalea* seamount is the more proximal structure to the coastline, rising  $\sim 260$  m from the seafloor (G–H in Figure 2b). The seamount has a size of  $10 \times 6$  km, and its upper surface is generally smooth and flat topped, with an outer edge located at depths of 200–236 m (G–H in Figure 2b). A subcircular pockmark, with a diameter of  $\sim 340$  m, is detected on the southwestern flank of the seamount.

The southern and northern seamount chains are separated by two ponded basins (B1 and B2 in Figure 2), connected through a 500-m structural high carved by narrow channels. The deeper basin (B1) extends over an area of  $170 \text{ km}^2$  and is delimited by the Palinuro-Glabro alignment to the south and by a  $15^\circ$  steep, 800-m-high scarp to the north. The basin B2 covers an area of  $80 \text{ km}^2$  and is bounded by two E-W oriented, steep and 100- to 200-m-high rectilinear scarps. This basin narrows toward NE forming a valley that bifurcates in two E-W elongated channels (Ch1 and Ch2 in Figure 2b). Noteworthy, a set of some km long and 10- to 40-m-high scarps aligned between  $N30$  and  $N35^\circ E$  are present in this sector (Figure 2b). These scarps strongly interact with the two channels, locally modifying their E-W direction (blue arrow in Figure 2b) or producing small knick points on their thalweg.

## 4.2. Seismic Lines

### 4.2.1. Seismo-Stratigraphic Analysis

Four main seismo-stratigraphic units, labeled as CCIV, UM, PQ, and V from bottom to top, were identified by their bounding unconformities and described on the base of their architecture and seismic characters (e.g., amplitude, lateral continuity, and frequency of internal reflectors, according to Damuth (1980)). Two distinctive seismic features, labeled as VM and LIPW, were likewise identified (Figures 3–5).

Unit UM has subparallel, discontinuous to semicontinuous, medium frequency, and high-to moderate-amplitude reflections. It is bounded at the top by the well-defined, high-amplitude horizon “M” (Figures 3b, 3d, and 4), a regional reflector associated with the top of evaporites deposited during the late Messinian salinity crisis and/or to an erosional unconformity formed during the late Messinian sea level fall (Malinverno et al., 1981). Unit UM is correlated with the Upper Miocene deposits.

Overlaying Unit PQ is characterized by layered, mostly continuous, medium- to high-frequency and moderate to high-amplitude reflections (Figures 3b–3d). It overlies the M horizon and its top, when detectable, corresponds to the sea bottom. Unit PQ can be correlated with the Plio-Quaternary sedimentary succession well developed in the whole Tyrrhenian sea (Bacini Sedimentari, 1980).

Discontinuous reflections of medium to high amplitude that may be interpreted as the seismic expression of volcanics characterize the Unit V (Figures 3b–3d, 4, and 5). Stratigraphically, it is embedded within PQ unit at different levels and may outcrop on the seafloor. The upper boundary of this unit corresponds to high amplitude, continuous to discontinuous reflections. It has a rough morphology and is marked by numerous diffraction hyperbolas.

Unit CCIV is characterized by chaotic reflections with several diffraction hyperbolas and bright spots (box 1 in Figure 4). The top of this unit shows a rough morphology. Unit CCIV stretches over the Diamante and Ovidio volcanic field as well as between them (Figures 3 and 4). Therefore, based on the seismic characteristics and position respect to the volcanic field, unit CCIV is interpreted as a basement composed of continental rocks largely intruded by magmatic material.

Further seismic features observed in the study area are VM and LIPW. Seismic feature VM generally exhibit a mound-shaped geometry, with a flat base and a convex top, discontinuous inner reflectors with anomalous seismic amplitude (Figure 3d). Based on the seismic expression and position respect to the volcanic field, they can be interpreted as volcanic mounds.

Feature LIPW shows a wedge shape with a well-defined edge (Figure 5d). Internally, reflectors show variable amplitude, high frequency, and sigmoid configuration. This feature can be interpreted as representative of the “Lowstand Infralittoral Prograding Wedge” (*sensu Hernández-Molina et al., 2000*) formed during relative sea level lowstands.

#### 4.2.2. Architecture of the DEOS Volcanic-Intrusive Complex

Basement continental rocks intruded by volcanics (Unit CCIV) has been interpreted throughout the areas beneath Ovidio and Diamante seamounts as well as between them and farther northwestward of the Diamante seamount (Figure 3b CDPs 1–5,500 and Figure 4b CDPs 350–1,500). The area, where Unit CCIV is recognized, is slightly folded to form an antiformal structure.

Upper Miocene deposits (Unit UM) are the oldest sedimentary deposits recognized outside the volcanic field, in the sector of the Paola Basin (Figure 3b CDPs 5,500–10,000 and Figure 4b CDPs 1–250) and at the base of the northwestern flank of the Diamante volcano (Figure 5b around the CDPs 1,500). The horizon M can be recognized beneath the E5c volcano (Figure 4b CDPs 250–500). Upper Miocene deposits and/or horizon M beneath other volcanic edifices cannot be inferred by our seismic lines. A sharp boundary between Unit UM deposits and the magmatic intrusion zone is observed in the Line Sinbus 1 around CDP 5,300 (Figure 3b).

Plio-Quaternary deposits (Unit PQ) are identified around the volcanic field and below the E5c volcano. Unit PQ reaches the maximum thickness of ~3.5 s. t.w.t. in the Paola Basin (Figures 3a and 3b around CDP 7,000), which may correspond to ~3,850 m. Unit PQ deposits thin moving from the Paola Basin northwestward, reaching ~1 s. t.w.t., (~1,100 m), just northwest of the E5c volcano (Figures 4a–4b around CDP 500). Here a sharp transition is observed between layered sedimentary deposits (Unit PQ) and volcanic rocks of E1 and E5 edifices (Figures 4a and 4b around CDPs 375 and 625). Unit PQ deposits can be inferred beneath the Ovidio seamounts (Figures 3a and 3b CDPs 1–5,500). However, here, it is not possible to define their base and top because the lateral continuity of reflectors is interrupted by the diffuse presence of magmatic intrusions.

Detachment surfaces and landslides are observed at different levels within PQ sedimentary in the area between Ovidio and Diamante volcanic edifices and farther to the NNW (Figures 5a and 5b CDPs 875–900 and CDPs 1,375–1,650, respectively). In this area, Unit PQ can be internally divided into two subunits by the reflector U1, which likely corresponds to a syntectonic erosional surface. The lower subunit PQ1 consists of parallel reflectors, dipping toward northwest while the upper subunit PQ2 has mostly horizontal reflectors.

A volcanic belt is inferred throughout the area beneath Ovidio and Diamante seamounts, above the upper continental crust strongly intruded by volcanics (Figures 3a–3b and 4a–4b). Volcanic rocks (Unit V) locally reach the seafloor forming volcanic edifices pertaining to the Diamante and Ovidio seamounts. Here

magmatic intrusions obscure at depth the seismic signal of Unit PQ and older sedimentary deposits. The only exception is beneath the E5c volcanic edifice, where the seismic expression of Unit PQ deposits is well preserved (Figures 4a and 4b around the CDP400). Sills are inferred on the base of the high-amplitude, continuous, and layered reflectors in the lower PQ sedimentary levels to the NW of the chimney of the E5c volcano (Figures 4a and 4b around the CDP 500).

Sedimentary deposits overlying the volcanics between Ovidio and Diamante seamounts are very thin (less than 250 m). On the contrary, they thicken northwestward of the Diamante volcano, where reach  $\sim 1.8$  s. t.w.t., corresponding to  $\sim 2,000$  m (Figures 4a and 5b CDPs 1,130–1,500). In this sector as well as to northwest of the E5c edifice, volcanic layers are interpreted at different sedimentary levels within the upper PQ unit.

Single magmatic mounds and associated structures, which include chimneys and lava flows, are interpreted within different upper PQ sedimentary levels in the eastern sector of the Paola Basin (Figure 3d). Volcanic mounds are observed in clusters around the E4 volcanic edifice (Figures 5a and 5b). Overall, they interrupt the lateral continuity of reflections of the Unit PQ. The height (up to 470 m), length (up to 1,100 m), stratal architecture and seismic characters of these mounds are quite variable. The seismic imaging is generally disturbed beneath the magmatic mounds due to the presence of chimneys. One distinctive feature recognized along the NNW flank of the E4 volcano is a  $\sim 1.4$ -km long and  $\sim 525$ -m thick pointed-top volcanic mound (Figures 5b and 5c). A funnel-shaped conduit is also observed beneath it.

Along the SSE side of the E4 volcano, a wedge-shaped feature is recognized (LIPW in Figure 5d). Its internal reflectors show a progradational geometry with a foreset slope up to  $18^\circ$ . The reflectors show toplap termination against the upper boundary that becomes an erosional surface landwards. The lower boundary of the LIPW is a downlap surface on the top of Unit V while the upper boundary is a toplap surface, inclined of  $\sim 2^\circ$ . The slope increases seaward up to  $20^\circ$ . Along the Line Sister 13, the LIPW is  $\sim 700$  m in length and 75 m in thickness. The present-day value for the depth of the edge of the LIPW is  $\sim 200$  m.

Three fault systems associated with positive flower structures are identified in the northwestern sector of the volcanic field (Figures 5a and 5b at CDPs 1,000–1,375). They offset both the volcanics and the sedimentary cover of the Diamante volcano and reach the sea floor. Generally, the faults are reverse with small offsets and converge at depth into a vertical fault. South-east dipping reverse and northwest dipping extensional faults are detected in the western and eastern flanks of the Diamante volcano, respectively (Figures 5a and 5b at CDPs 1,500–1,650 and 850–1,000). In particular, one of these normal faults reaches the sea floor (Figures 5a and 5b around CDP 900). Furthermore, a southwest dipping, extensional fault cuts reflectors at the upper level of Unit PQ in the Paola Basin (Figures 3a and 3b around CDP 6,500).

### 4.3. Magnetic Anomalies and Modeling

Anomaly A is the largest magnetic dipole of the NOCA overlapping the DEOS area. This anomaly is characterized by a direct polarity and likely derives from the superimposition of almost three magnetic subanomalies, namely A-1, A-2, and A-3, placed 14 km apart (Figures 6a and 6b). The grid of the magnetic surveys was not suitably dimensioned with respect to the wavelengths of these subanomalies (around 5–10 km), and it does not properly define each feature separately. As an example, the A3 feature forms a separated southwestern undulation of the anomaly-A and it lies just where the survey grids enlarge (inset Figure 6b). Consequently, the modeling and the interpretative considerations about the anomaly A have to be taken as a general and rough description of the reality.

The subanomalies A-1 and A-2 show two strike directions (Figure 6b). To the east, the subanomaly A-1 has a higher intensity and longer wavelength (10 km), shows EW and NE-SW orientations, and overlaps the Ovidio seamounts as well as the valley separating Enotrio and Diamante seamounts. The peak of this sub anomaly is about 130 nT, whereas the surrounding eastern area is generally about  $-20$  nT. To the west, the lower intensities and shorter wavelengths A-2 and A-3 subanomalies are about 55 and 15 nT, respectively (Figure 6b).

The RTP-TMI field of anomaly A shows a 3-km shift of the positive magnetic peaks northward (Figure 6c). The RTP-TMI field displays a better localization and isolation of the three magnetic features with respect to the TMI field (Figures 6b and 6d). The RTP-A-1 subanomaly strikes mainly in the EW direction and rotates to the NE-SW (south-western border), overlapping the northern edge of the Ovidio seamounts (E2–E4 edifices and the small cones C3–C4 in Figure 3) and the southern flank of the valley dividing Diamante-Scalea



chain from Ovidio seamounts. The RTP-A-2 subanomaly is elongated in EW direction and extends almost entirely in the area of the Diamante seamount. The RTP-A3 subanomaly is a well-rounded and isolated feature at the northern flank of the Enotrio seamount. Both TMI and RTP-TMI fields of subanomaly A-1, show a northern, eastern, and southern boundary with a steep magnetic gradient. On the contrary, subanomalies A-2 and A-3 have a gentler decrease in the magnetic field.

The inverse modeling results are shown as 2-D  $xy$  depth slices (Figures 7a–7d) and as a 3-D perspective (Figures 7f–7i), where the 0.01 k-SI isoline and isosurface can be approximately considered as the external source boundary encompassing most of the rock volume with meaningful magnetic properties. The 3-D image highlights the source geometry and its relationship with the seafloor. The obtained model has been evaluated on the base of its agreement with the geostructural framework of the area as well as its dimensional parameters (e.g., the model norm, smoothness, and misfit). Particularly, the differences between observed and predicted data (Figures 6d–6e) do not show marked misfit trends, and it implies error ranges of  $-1.0 < nT < 0.7$  in correspondence of the anomalies peak area (Figure 6f). Therefore, anomaly A and its subanomalies are well solved by the inversion, and the error range represents the 1.1% of the TMI intensity actual intervals. The obtained susceptibility ranges  $0.0077 < k\text{-SI} < 0.019$ , corresponding to a magnetization range of about  $0.3 < A/m < 0.7$  for the inducing field of the time of the survey of  $F = 44,900$  nT (IGRF 1978; [www.ngdc.noaa.gov/](http://www.ngdc.noaa.gov/)).

The A-1 source lies in correspondence of the northwestern part of the Ovidio seamounts. It has a remarkable extension in depth, ranging from the seafloor (or from very shallow levels) down to  $-6$  km (Figures 7a, 7b, and 7f). Because of the regional scale of the data set, the magnetic modeling is not able to completely separate the A-1 and A-2 sources at depth (Figures 7c and 7d). The saddle between them may likely highlight the end of a source and the start of another one. The A-1 source shows a complex geometry characterized by an EW  $\sim 11$ -km-elongated central trunk below the E3–E4 edifices (between 2.3 km and the model bottom; Figures 7e–7h). This portion of the source is aligned with (1) B1–B2 basins, (2) the valley to the NE of B2 basin, and (3) the Glabro-Enotrio and Diamante-Scalea chains. In the deeper part, the A-1 source enlarges toward east and southwest (Figures 7c and 7d). Instead, at shallower depths (between  $-800$  and  $-2,400$  m; Figures 7a and 7b) the source is characterized by two lateral branches (southwestern and southeastern). The source upper surface gently dips in the north and western directions, whereas it has a steep southern flank just below E2–E4 (Figures 7e–7h). The eastern flank has an arch-like shape geometry which mimics the sequence of the surficial edifices. The northwestern side is positioned below the final portion of the valley, facing the Diamante seamounts.

The A-2 source displays almost the same extension of the Diamante seamount. Its top lies roughly at  $\sim 1,900$  m bsl below the higher Diamante crest. Instead its bottom lies at  $\sim -5$  km (Figures 7b–7d). This source is mainly elongated in WNW-ESE direction, parallel to the Diamante seamount, and maintains its strike at depth. The A-2 source is characterized by lower magnetic properties respect to the A-1 source and ranges  $0.0067 < k\text{-SI} < 0.013$  (corresponding to an induced magnetization ( $J_i$ ) range of  $0.2 < A/m < 0.5$ ).

The A-3 anomaly has a weak intensity in comparison with the A-1 and A-2. It lies along the Enotrio northern side and exhibits a well-rounded shape with a wavelength smaller than the Enotrio extension (about 5.8 km; Figures 6b and 6c). The inverse model does not properly determine the A-3 anomaly because of the low resolution of the data. Thus, it was removed by the calculation. However, we can speculate that this source should be positioned in the shallower crustal depths between 1 and 2 km based on its characteristics.

#### 4.4. Local Earthquake Tomography

$P$  wave velocity plates at 3-, 6-, and 9-km depth indicate that the whole resolved area is characterized by high-velocity values (Figure 8), with variations greater than 8% with respect to the starting model. In this high-velocity domain, the target area (see the box in the figure) shows nil-to-moderate variations ( $\sim 0\%$  to  $2\%$ ) that tend to increase in the northwestern sector. The vertical section A shows that the southern sector, including the sections C and D, is characterized by lower velocity values than the northern one (north of sections C approximately). This pattern is further highlighted by the E-W oriented vertical sections suggesting that the area of relatively low-velocity values, already observed in the plates at 3- to 9-km depth, is mainly located in the southern portion of the target area (i.e., in the Enotrio-Ovidio sector;

sections D and C), and its extension is reduced to the north (section B) where it appears mainly confined in the central-eastern sector of the target area (approximately east of section A). The seismic activity is almost exclusively located in the northwestern portion of the target area, just where the velocity values increase.

Figure 8 (bottom) shows that the Diamante, Enotrio, and Ovidio seamounts are located in correspondence to a low  $V_p/V_s$  anomaly, reaching minimum values of about 1.66. Focusing on the results at 3- to 9-km depth, the anomaly is well defined in almost all the target area, except for the northwestern portion (approximately in the Diamante sector) where most of the seismic activity occurs. The low  $V_p/V_s$  values are still visible moving toward deeper depths (i.e., 18- and 27-km depth), but they seem to indicate a regional domain rather than an isolated anomaly (i.e., low  $V_p/V_s$  values are diffused in most of the layer). According to the map view, the vertical section A shows that the low  $V_p/V_s$  anomaly covers almost all the target area from south to north (see the intersections with sections B–D). The joint evaluation of W–E oriented vertical sections highlights the smaller extension of the low  $V_p/V_s$  anomaly in the northernmost section B, where it seems to be mainly located in the eastern portion of the target area and reduces in the western one (e.g., west of section A). The lowest values are found in section C where it is also evident that the seismicity tends to occur outside of the low  $V_p/V_s$  anomaly.

## 5. Discussion

The above described geophysical data show a previously unknown (except for the western part of Ovidio seamounts) volcanic-intrusive complex in the eastern prolongation of the Palinuro–Glabro chain consisting of volcanic seamounts and of a shallow zone of magmatic intrusions and subvertical conduits. In the following, we discuss (a) the volcanic nature of the seamounts and the age of volcanism, (b) the interplay between volcanism, sea-level change, erosion and sedimentation, and (c) the mechanism responsible for the volcanism within the frame of the geodynamic evolution of the Tyrrhenian–Ionian subduction system.

### 5.1. Volcanic Nature and Age of the DEOS and Scalea Seamount

The volcanic nature of the DEOS is witnessed by the typical morphologies of the seamounts, the analysis of seismic facies, the existence of magnetized material as well as by the 3-D velocity model. Moreover, sheet and pillow lavas were observed through ROV dives on the top of the Ovidio (E1 in Figure 3) seamount (Cocchi et al., 2017).

The 11-km-long A-1 source represents the largest magnetic contrast generating the composite A-dipole (Figures 6 and 7). Its directions of elongation (E–W and NE–SW) at shallower depths (Figures 7a and 7b), roughly correspond to the alignment of the E2, E3, and E4 edifices. Therefore, the geometrical relationship between the seamounts and the A-1 source below them suggest that the magnetized material corresponds to crystallized magma belonging to the seamounts feeding system. At deeper depth (Figures 7b and 7c), the A-1 source direction of elongation does not change substantially. The A-1 source is laterally displaced with respect to the surficial volcanic structures. It gently dips to the northwest and to the west, whereas it has a vertically elongated shape just below the E2–E4 edifices (Figures 7e–7h). Thus, we interpret it as the main-stream of inclined conduits-dikes swarms which fed the surficial volcanic activity (Figures 3 and 7e–7h). Oblique dipping magma feeding systems and magma chambers, positioned in offset with respect to their volcanic centers, have been documented worldwide by geophysical studies (Aizawa et al., 2014; González et al., 2013; Ishizuka et al., 2008) and indicate a lateral transportation of the magma, influenced by the tectonics (Tibaldi, 2015). The volcanic nature of the DEOS is also corroborated by all seismic lines that shows a typical seismic signature of volcanic rocks below the E1 and E4 edifices and several magmatic intrusions that reach the sea-floor in the area extending between these edifices and the Diamante volcano. The Line Crop M36 (Figures 4a and 4b) also shows volcanic chimneys underlying the E1 and E5c edifices. The presence of these features suggests that the area of magma ascent is wider respect to the A-1 source, although not all the volcanic seamounts and intrusions are magnetized. Evidence of lava flows and laccoliths are mostly confined in the northernmost part of the Paola Basin, indicating that the ascent of magma is reduced moving toward the east.

The A-2 source has the same size and strike of the Diamante seamount, and its upper part lies significantly below this edifice (Figures 7e–7h). Moreover, both the Crop M36 and Sister 13B lines (Figures 4 and 5) show

a seismic signature typical of volcanic rocks topped by sediments in the area corresponding to the Diamante seamount. In this context, it is reasonable to consider the A-2 source as the magnetized part of the Diamante volcanic feeding system.

The A-3 subanomaly lies in correspondence of the northern side of the Enotrio seamount, and it was not solved by the magnetic data inversion. However, the position and wavelength of this anomaly (Figures 6b and 6c) suggest it may belong to the previously described intruded volcanic magnetized material beneath the Diamante seamount. The volcanic nature of Enotrio is also suggested by sheet lava flows and subvertical dikes observed by ROV at the top of this seamount (Cocchi et al., 2017).

The inverse modeling we carried out is affected by the low resolution of the data set (regional scale; Figure 6a). Furthermore, in this area, the magnetic anomaly field is deformed by the lowering effect of the PVC negative lobe (Figure 6a). Although this latter effect is not quantifiable, the obtained model would have susceptibility values significantly higher. Nevertheless, the achieved geometries and depth ranges are well in agreement with the geostructural and seismic data.

The other Ovidio seamounts (E1 and E5a–E5c; Figure 2b) do not show any magnetic signature (Figures 6b–6c), even though this condition may be related to the resolution of our data set which does not sample shorter wavelengths of shallower-outcropping sources. Their volcanic nature is also suggested both by the presence of deep-seated chimneys beneath them (Figures 3b and 4b) and by their morphology (e.g., the arc-like shape rim at the summit of the E5c edifice in Figure 2b).

The direct polarity of the composite magnetic anomaly A suggests that the volcanic edifices and the emplacement of these magnetic sources most likely occurred during the Brunhes Chron. Thus, the DEOS activity should be younger than 0.7 Myr. Our data also indicate that most of the volcanic activity ended, even if small magma ascents are observable in the Line Sister 13B (Figures 5a and 5b) and in two sites on the top of the Ovidio E1 volcanic edifice (Figures 4a and 4b). A further age constraint, indicating a pre-Last Glacial Maximum activity, is derived by the occurrence of the LIPW around the edifice E4. It is also worthy of note the net decrease of the magnetic anomaly field intensities from the PVC moving eastward to DEOS. In correspondence of the PVC, the TMI is about 500 nT (Cocchi et al., 2017), while in the Ovidio seamounts is about 150 nT (Figures 6a and 6b). The eastward decrease of the magnetic properties may likely be related to (1) a high heat flux caused by the local hydrothermal system related to the Ovidio seamounts and (2) a net change in the volcanic product geochemistry (less content in ferromagnetic minerals) and increase in the ratio between volcanoclastic and lava flows going from deeper to shallow water, where explosive activity predominates. In the first case, high heat flux lowers the magnetic properties bringing the temperature close or above the Curie Temperature (Vacquier, 1972).

The presence of pockmarks and bathymetric lows (e.g., P and DEP features in Figure 2b), as well as the low  $V_p/V_s$  ratio in the first 9-km depth, indicating fluid-filled rocks beneath the Ovidio seamounts likely related to a magma-cooling process, and the presence of thermal baths along the seashore (es. *Terme Luigiane* village in Figure 2a) would support the hypothesis of existence of a hydrothermal system. In particular, the morphology of giant depressions is similar to fluid-escape depressions recently reported in the Tyrrhenian Sea and associated to hydrothermal venting (Ingrassia et al., 2015; Martorelli et al., 2016). In the second case, the different tectonic conditions along the Glabro Diamante Enotrio seamounts may have caused differentiation processes in the upwelling magmas causing chemical modifications toward more felsic and less magnetic products (Reynolds, 2011).

It is also worth to note that the surficial volcanic morphology varies moving from the Diamante-Enotrio to the Ovidio seamounts (Figure 2). The shape of the former seamounts appears to be mostly controlled by the tectonics, whereas the geometry of the latter seamounts seems to directly reflect the constructive volcanic form. In both cases, the surficial and deep magnetic sources are directly related to the E-W STEP fault.

For what concerns the Scalea seamount (Figure 2a), it does not show any magnetic properties, and it is not crossed by seismic profiles. Nevertheless, considering the proximity of this seamount to Ovidio and Diamante and its E-W elongated flat-topped morphology, similar to the other edifices, we speculate that it has a volcanic origin.



## 5.2. Interplay Between Volcanism, Sea-Level Changes, Erosion, and Sedimentation

The morpho-bathymetric map allows to distinguish a western, deeper sector dominated by volcanic edifices with a rugged morphology and an eastern shallower sector where volcanic edifices have a smoother and mostly flat-topped morphology. We analyze the latter edifices to understand if the flat-topped morphology has a constructional origin or results from wave erosion processes, due to the interplay between the Late Quaternary eustatic sea level changes and vertical movements.

Flat-topped cones and/or lava terraces linked to constructional volcanic process are recognized in the deeper (typically >700 m bsl) part of submarine volcanic ridges, such as Reykjanes Ridge, Puna Ridge, Hawaiian Archipelago, and Galapagos (Clague et al., 2000; Parson et al., 1993; Smith & Cann, 1999). In fact, the long-lived steady effusive eruption with low volatile contents and moderate to high confining pressures are considered main factors in promoting the construction of flat-topped landforms. Considering (a) the depth of the Scalea and Ovidio seamounts between ~200 and 500 m bsl, (b) the presence of subconcentric ridges and small circular highs on the summit of the edifices, generally interpreted as remnants of wave-eroded central vents (Casalbore et al., 2015; Chiocci et al., 2013; Coltelli et al., 2016; Cuffaro et al., 2016; Kokelaar & Durant, 1983; Romagnoli & Jakobsson, 2015; Schwartz et al., 2018), and (c) the presence of a progradational sedimentary body, which is a shallow-water indicator, on the flank of the edifices E4, we suggest the flat-topped morphology as originated by wave erosion. This process was invoked by several authors in order to explain the origin of subsiding insular and oceanic volcanoes (e.g., Quartau et al., 2014; Romagnoli et al., 2018) or seamounts (e.g., Cuffaro et al., 2016; Tempera et al., 2013). A similar interpretation is proposed to explain flat-top surfaces of the PVC by Cocchi et al. (2017) and Passaro et al. (2010). Differently, the interpretation of the flat-topped edifice E1 is more complex, because it shows a more articulated morphology of its top (profile C-D in Figure 2) compared to the other edifices. Particularly, its summit is characterized by a mounded and stepped morphology (stepped mound in Figure 2b) in the eastern part that is up to 200 m higher than the flatter western part (left part of the profile C-D in Figure 2), suggesting that this volcanic edifice has been characterized by different stages of construction and erosion during its recent evolution. Indeed, a few ROV observations on the summit of E1 showed outcropping sheet and pillow lavas (Cocchi et al., 2017), suggesting a more recent volcanic activity or a minor wave erosion during sea-level fluctuations. Based on such evidence, its flat-top surface was supposed by Cocchi et al. (2017) not to be originated by wave erosion because it resembles that of mid-ocean ridges and submarine Hawaiian volcanoes, which grow by long-lived steady eruptions with low effusion rates. Also, the observation of outcropping sheet and pillow lavas on the seabed (Cocchi et al., 2017) could suggest a more recent volcanic activity or a minor wave erosion during sea-level fluctuations.

The LIPW (Figure 5d) formed seaward of the lower edge of abrasion platforms under the combined action of the local storm-wave base level and across-shore currents (Mitchell et al., 2012). Thus, it can be used as a paleo sea level indicator to infer vertical tectonic motion (Casalbore et al., 2017; Chiocci & Orlando, 1996; Pepe et al., 2014). By considering that (a) the depth of LIPW recognized in the flank of the E4 is 200 m, (b) the depth of LIPW formation is estimated around 20 m for the Tyrrhenian Sea (Pepe et al., 2014), and (c) the minimum sea level reached during the Late Quaternary fluctuations was about 120 m below the present level (Bintanja et al., 2005), it is reasonable to assume that the area where the E4 volcano formed experienced at least 60 m of subsidence. It is noteworthy that the depth of the flat-topped volcano summits of the Ovidio seamounts progressively increases from the E4 (and Scalea seamount) to E1 suggesting that the amount of subsidence increase moving westward. The latter is also corroborated by the overall tilting westward of the summit area of most of the flat-topped edifices (E1, E2, E3, and E5b in Figure 2b). This could suggest that trench rollback and low coupling is associated with the topographic sinking of the upper plate of the Tyrrhenian-Ionian subduction system.

## 5.3. Geodynamic Implication

The subducting Ionian slab retreated southwestward for about 400 km from the Late Neogene to recent and decreasing its width to the present-day shape. The retreat of the Ionian slab together with its rollback caused the opening of back-arc basins inside the Tyrrhenian domain and created a complex three-dimensional, time evolving, mantle return flows characterized by poloidal and toroidal mantle circulation, which develop according to the slab geometry and rollback rate (Faccenna et al., 2010, 2011; Funicello et al., 2006; Király et al., 2017). When the slab return flow interacts with a hydrated layer in the transition zone

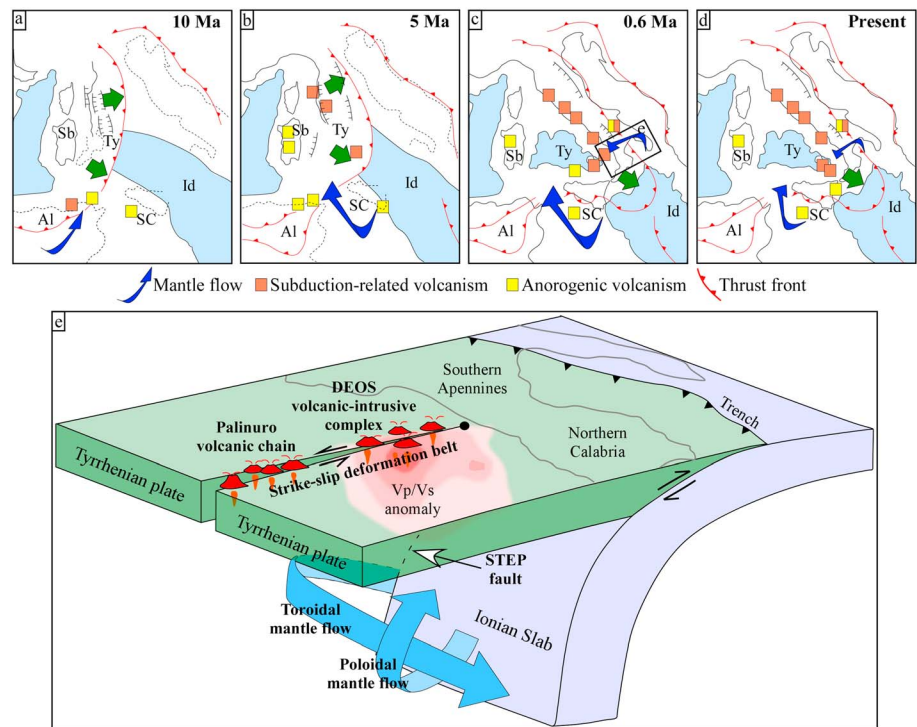


**Figure 9.** (a–d) Reconstruction of the evolution of the Central Mediterranean subduction zone back over the last 10 Ma (modified from Faccenna et al., 2004; Faccenna et al., 2010). Green arrows indicate the active thrust front. For each frame, we show only the active volcanism. Abbreviations: Al, Algerian margin; Io, Ionian domain; Sb, Sardinia block; SC, Sicily Channel; Ty, Tyrrhenian domain. (e) Three-dimensional geodynamic sketch of the Tyrrhenian-Ionian subduction system that illustrates mantle flow path (poloidal and toroidal) around the deforming Ionian slab, and the Palinuro volcanic chain and DEOS volcanic-intrusive complex formed along the northern edge of the Ionian slab as a consequence of subduction-induced mantle flow (see text for details). DEOSs = Diamante, Enotrio, and Ovidio seamounts; STEP = Subduction-Transform Edge Propagator.

(Leahy & Bercovici, 2007), plume-like mantle upwelling occurs (Faccenna et al., 2010) giving place to important implications such as the off-arc volcanism described by Király et al. (2017).

The formation and evolution of the DEOS volcanic-intrusive complex is discussed in the frame of the deformation history of the Ionian slab and the mantle flow path (Figures 9a–9d) by combining our data with those available in the literature (Chiarabba et al., 2008; Faccenna et al., 2010, 2005, 2004; Lucente et al., 1999; Neri et al., 2012; Piromallo & Morelli, 2003; Wortel & Spakman, 2000). We identified four episodes of slab deformation during the last 10 Ma.

At around 10 Ma, the position of the trench was located east of the Sardinia block and the opening of the Tyrrhenian basin started (Figure 9a). At this time, calc-alkaline volcanism took place over the Algerian margin as a consequence of the mantle upwelling that fed the magmatism above the eastern edge of the Algerian slab. Eastward, alkali-basalt volcanism developed in the area of the future Sicily Channel.

Between 10 and 5 Ma, rifting migrated eastward within the Tyrrhenian domain for about 300 km (Figure 9b). There, the velocity of extension increased as a consequence of the break of the slab along the future Sicily Channel. From this time onward, a segment of the slab migrates southward in northern Africa while the other one retreated toward the southeast in Calabria. In the Tyrrhenian domain, the formation of the slab window was marked by the sea-floor spreading in the Vavilov back-arc basin and the formation of subduction-related volcanism in the future Tyrrhenian Sea. Anorogenic volcanisms also occurred in the northern Tunisia, Sardinia, and along the future Sicily Channel (Figure 9b).

Between 5 and 0.6 Ma, the rifting continued the south-eastward migration within the Tyrrhenian domain (Figure 9c). The seafloor spreading jumped southeastward into the Marsili back-arc basin, and oceanic crust emplaced since 1.87–1.67 Ma.

Around 0.6 Ma, a STEP fault associated with lateral lithospheric tearing formed at the northern edge of the Ionian slab (Figure 9e). Based on the tomographic images (e.g., Rosenbaum et al., 2008) and seismic reflection data available in the Ionian Abyssal Plain and surroundings (Catalano & Sulli, 2006; De Voogd et al., 1992; Finetti & Del Ben, 1986), we propose that this STEP fault developed along the transition zone between subducting segments of continental (Adriatic) and oceanic (Ionian) lithosphere (Figure 1d). The difference of the nature of the subducting slab could explain the different amount of backward migration and, as a consequence, the breaking of the subducting lithosphere into narrow slab segments through slab tearing.

The segmentation of the subduction zone produces a complex pattern of mantle circulation around them that was responsible for the formation of subduction-related volcanism in the eastern side of the Tyrrhenian domain (Figure 9c). By considering that the STEP faults played an important role in controlling the magma uprising in the whole eastern side of the Tyrrhenian domain (Rosenbaum et al., 2008), we propose that the formation and upwelling of subduction-induced mantle flow that fed the PVC and DEOS volcanic-intrusive complex was controlled by the STEP fault that limits the northern edge of the Ionian slab. Eastward of DEOS, only thermal springs occur (Figure 2a). Here the lack of volcanism can be explained by considering that below this sector the subducting slab lies at shallow depth, and thus, the overlying mantle material is not into the zone of hydration, where the decompression melting occurs.

The DEOS volcanic-intrusive complex developed within a strike-slip deformation belt that accommodated the bulk of the shear strain along the roughly E-W trending STEP fault (Figure 9e). Thus, the ascent of the melts and its final emplacement was favored by transpressive and transtensive deformation.

The dredged rocks have a calc-alkaline affinity (Trua et al., 2004, and references therein) and show an island arc basalt signature (Cocchi et al., 2017). The geochemical evidence, integrated with structural data and geodynamic constraints, suggest a modification of the mantle source by crustal components. Thus, the formation of the PVC can be associated with subduction-related volcanism (*sensu* Lustrino & Wilson, 2007). By considering that the DEOS volcanic-intrusive complex represents the eastern prolongation of the PVC, we speculate that it is also characterized by subduction-related volcanism. Conversely, anorogenic volcanism scattered in Sardinia, southern Tyrrhenian Sea, eastern Sicily, and Sicily Channel (Figure 9c).

At present (Figure 9d) the mantle upwelling feeding the DEOS volcanic-intrusive complex stopped. We propose that the end of the subduction-related volcanism above the northern edge of the Ionian slab is a consequence of the reduction of the mantle flow circulations due to the decreasing of slab rollback (Goes et al., 2004) and to the Ionian slab break off beneath the northern Calabrian Arc (Buiter et al., 2002; Westaway, 1993; Wortel & Spakman, 2000) during the Middle-Late Pleistocene. Conversely, the subduction-related volcanism continues ahead of the slab (Aeolian Arc), along the eastern sector of the Tyrrhenian domain (Figure 9d). Anorogenic volcanism also occurs in the eastern Sicily, Sicily Channel, and Sardinia.

## 6. Conclusion

The integrated analysis of different geophysical data sets provides for the first-time evidence of a magmatic volcanic complex developed in the offshore of the northern Calabrian Arc (Southern Tyrrhenian Sea). Our results, integrated with data derived from the literature, are relevant for understanding the magmatic response to the slab tearing occurred in the Tyrrhenian-Ionian Subduction System and provide new insights on the evolution of subduction-induced mantle flow around the slab edges. The main outcomes can be summarized as follows:

1. A volcanic-intrusive complex is identified in an area located about 15 km off the Tyrrhenian coast of the northern Calabria. The edifices are off-axis respect to the main feeding system of this volcanic complex and in correspondence of a shallower crustal volume characterized by low  $V_p/V_s$  ratios. Magmatic intrusions reaching the sea floor, chimneys, lava flow, and laccolith are observed in the area beneath and surrounding the volcanoes. The emplacement and cooling of the magma occurred during the Brunhes Chron. Presently, the volcanoes are not active even if small magma ascents are still observable.
2. The volcanic-intrusive complex can be subdivided in a western domain where strike-slip transpressional faults deform the volcanic edifices and control the seafloor landscape (Diamante and Enotrio seamounts) and an eastern domain characterized by flat-topped volcanic edifices (Ovidio seamounts). The flat-topped morphology is mostly the results of the interplay between volcanism and sea-level changes that



cause erosion and sedimentation. The Ovidio seamounts formed in an area that experienced at least 60 m of tectonic subsidence. Subsidence is likely to increase from the east to the west.

3. The decompression melting of mantle material originated the magma responsible for the formation of the volcanic-intrusive complex occurred at the northern edge of the Ionian slab whereas a roughly E-W trending STEP fault exerted a direct control on the magma uprising.

## Author Contributions

Study conception and design: De Ritis R., Pepe F., Casalbore D., Orecchio B.; analysis and interpretation of seismic data: Pepe F., Corradino M., Nicolich R.; analysis, modeling and interpretation of magnetometric data: De Ritis R., Chiappini M.; earthquake data collection, tomographic inversion, and interpretation: Orecchio B., Presti D., Totaro C. acquisition, processing, and analysis of multibeam data: Bosman A., Casalbore D., Chiocci F., Martorelli E.; drafting of manuscript: Pepe, De Ritis R., Casalbore D., Corradino M., Orecchio B.; joint evaluation of all the results in the regional geodynamic framework: all authors critical revision: all authors.

## Acknowledgments

We would acknowledge crews of R/V Urania, Maria Grazia, and Minerva (CNR) together with the researchers and students that have taken part to the oceanographic cruises. We would like to thank Michael Marani, an anonymous reviewer, for his constructive comments. Thanks also to the Editor (Laurent Jolivet) and Associate Editor (Paola Vannucchi) for carefully evaluating our work. High-resolution multibeam bathymetry was acquired by CNR in the framework of the Marine Geohazard along the Italian Coast (MaGIC) Project. The multibeam bathymetry data are available at <http://portal.emodnet-bathymetry.eu/> website; the multichannel seismic data are available at [www.epaf.eu](http://www.epaf.eu) website; regional magnetic anomalies data can be obtained from published literature, listed in the references; seismological data are available at [www.ingv.it](http://www.ingv.it) website. We thank the EMODnet Bathymetry Consortium (2016) for providing the part of the multibeam data set. Interpretation of seismic profiles was conducted using the GeoSuite All Works software package. This study has been partly funded by the Ministero degli Affari Esteri e della Cooperazione Internazionale in the frame of EPAF Project. Bathymetric data were collected in research projects funded by the National Research Council.

## References

- Agip, S. (1981). Italia, Carta Magnetica: Anomalie del Campo Magnetico Residuo. In S. Donato Milanese.
- Aizawa, K., Koyama, T., Hase, H., Uyeshima, M., Kanda, W., Utsugi, M., & Yamazaki, K. (2014). Three-dimensional resistivity structure and magma plumbing system of the Kirishima Volcanoes as inferred from broadband magnetotelluric data. *Journal of Geophysical Research: Solid Earth*, *119*, 198–215. <https://doi.org/10.1002/2013JB010682>
- Argnani, A. (2009). Evolution of the southern Tyrrhenian slab tear and active tectonics along the western edge of the Tyrrhenian subducted slab. *Geological Society, London, Special Publications*, *311*(1), 193–212. <https://doi.org/10.1144/SP311.7>
- Argnani, A., & Savelli, C. (1999). Cenozoic volcanism and tectonics in the southern Tyrrhenian sea: Space-time distribution and geodynamic significance. *Journal of Geodynamics*, *27*(4–5), 409–432. [https://doi.org/10.1016/S0264-3707\(98\)00025-8](https://doi.org/10.1016/S0264-3707(98)00025-8)
- Argnani, A., & Trincardi, F. (1988). Paola slope basin: Evidence of regional contraction on the eastern Tyrrhenian margin. *Memorie Della Società Geologica Italiana*, *44*, 93–105.
- Baccheschi, P., Margheriti, L., & Steckler, M. S. (2007). Seismic anisotropy reveals focused mantle flow around the Calabrian slab (Southern Italy). *Geophysical Research Letters*, *34*, L05302. <https://doi.org/10.1029/2006GL028899>
- Baes, M., Govers, R., & Wortel, R. (2011). Subduction initiation along the inherited weakness zone at the edge of a slab: Insights from numerical models. *Geophysical Journal International*, *184*(3), 991–1008. <https://doi.org/10.1111/j.1365-246X.2010.04896.x>
- Baranov, V., & Naudy, H. (1964). Numerical calculation of the formula of reduction to the magnetic pole. *Geophysics*, *29*(1), 67–79. <https://doi.org/10.1190/1.1439334>
- Barberi, F., Gasparini, P., Innocenti, F., & Villari, L. (1973). Volcanism of the southern Tyrrhenian Sea and its geodynamic implications. *Journal of Geophysical Research*, *78*(23), 5221–5232. <https://doi.org/10.1029/JB078i023p05221>
- Barreca, G., Corradino, M., Monaco, C., & Pepe, F. (2018). Active tectonics along the south east offshore margin of Mt. Etna: New insights from high-resolution seismic profiles. *Geosciences*, *8*(2). <https://doi.org/10.3390/geosciences8020062>
- Beccaluva, L., Gabbianelli, G., Lucchini, F., Rossi, P. L., & Savelli, C. (1985). Petrology and K/Ar ages of volcanics dredged from the Eolian seamounts: Implications for geodynamic evolution of the southern Tyrrhenian basin. *Earth and Planetary Science Letters*, *74*(2–3), 187–208. [https://doi.org/10.1016/0012-821X\(85\)90021-4](https://doi.org/10.1016/0012-821X(85)90021-4)
- Bintanja, R., van de Wal, R. S. W., & Oerlemans, J. (2005). Modelled atmospheric temperatures and global sea levels over the past million years. *Nature*, *437*(7055), 125–128. <https://doi.org/10.1038/nature03975>
- Blakely, R. J. (1996). *Potential theory in gravity and magnetic applications*. Cambridge University Press.
- Boccaletti, M., Nicolich, R., & Tortorici, L. (1984). The Calabrian Arc and the Ionian Sea in the dynamic evolution of the Central Mediterranean. *Marine Geology*, *55*(3–4), 219–245. [https://doi.org/10.1016/0025-3227\(84\)90070-7](https://doi.org/10.1016/0025-3227(84)90070-7)
- Buiter, S. J. H., Govers, R., & Wortel, M. J. R. (2002). Two-dimensional simulations of surface deformation caused by slab detachment. *Tectonophysics*, *354*, 195–210.
- Carminati, E., Cavazza, W., Roure, F., Spakman, W., Stampfli, G. M., & Ziegler, P. A. (2004). TRANSMED Transect III: Massif Central-Provence-Gulf of Lion-Provençal Basin-Sardinia-Tyrrhenian Basin-Southern Apennines-Apulia-Adriatic Sea-Albanides-Balkans-Moesian Platform. In W. Cavazza, F. S. Roure, G. M. Stampfli, & P. A. Ziegler (Eds.), *The TRANSMED Atlas: The Mediterranean Region from Crust to Mantle* (Chap. 1, pp. 1–15). Heidelberg: Springer-Verlag.
- Carminati, E., & Doglioni, C. (2005). *EUROPE/Mediterranean Tectonics, Encyclopedia of Geology*. Academic Press. <https://doi.org/10.1016/B0-12-369396-9/00135-0>
- Carminati, E., Wortel, M. J. R., Spakman, W., & Sabadini, R. (1998). The role of slab detachment processes in the opening of the western-central Mediterranean basins: Some geological and geophysical evidence. *Earth and Planetary Science Letters*, *160*(3–4), 651–665. [https://doi.org/10.1016/S0012-821X\(98\)00118-6](https://doi.org/10.1016/S0012-821X(98)00118-6)
- Caratori Tontini, F., Stefanelli, P., Giori, I., Faggioni, O., & Carmisciano, C. (2004). The revised aeromagnetic anomaly map of Italy. *Annals of Geophysics*, *47*(5).
- Casalbore, D., Falese, F., Martorelli, E., Romagnoli, C., & Chiocci, F. L. (2017). Submarine depositional terraces in the Tyrrhenian Sea as a proxy for paleo-sea level reconstruction: Problems and perspective. *Quaternary International*, *439*, 169–180. <https://doi.org/10.1016/j.quaint.2016.02.027>
- Casalbore, D., Romagnoli, C., Pimentel, A., Quartau, R., Casas, D., Ercilla, G., & Chiocci, F. L. (2015). Volcanic, tectonic and mass-wasting processes offshore Terceira Island (Azores) revealed by high-resolution seafloor mapping. *Bulletin of Volcanology*, *77*(3), 24. <https://doi.org/10.1007/s00445-015-0905-3>
- Catalano, R., & Sulli, A. (2006). Crustal image of the Ionian basin and accretionary wedge. *Bollettino Di Geofisica Teorica Ed Applicata*, *47*(3), 343–374.

- Cernobori, L., Hirn, A., McBride, J. H., Nicolich, R., Petronio, L., & Romanelli, M. (1996). Crustal image of the Ionian basin and its Calabrian margins. *Tectonophysics*, 264(1–4), 175–189. [https://doi.org/10.1016/S0040-1951\(96\)00125-4](https://doi.org/10.1016/S0040-1951(96)00125-4)
- Chatelain, J., Molnar, P., Prévot, R., & Isacks, B. (1992). Detachment of part of the downgoing slab and uplift of the New Hebrides (Vanuatu) Islands. *Geophysical Research Letters*, 19(14), 1507–1510. <https://doi.org/10.1029/92GL01389>
- Chiappini, M. (2000). Onshore-offshore integrated shaded relief magnetic: Anomaly map at sea level of Italy and surrounding areas. *Annali Di Geofisica*.
- Chiarabba, C., De Gori, P., & Speranza, F. (2008). The southern Tyrrhenian subduction zone: Deep geometry, magmatism and Plio-Pleistocene evolution. *Earth and Planetary Science Letters*, 268(3–4), 408–423. <https://doi.org/10.1016/j.epsl.2008.01.036>
- Chiocci, F. L., & Orlando, L. (1996). Lowstand terraces on Tyrrhenian Sea steep continental slopes. *Marine Geology*, 134(1–2), 127–143. [https://doi.org/10.1016/0025-3227\(96\)00023-0](https://doi.org/10.1016/0025-3227(96)00023-0)
- Chiocci, F. L., Romagnoli, C., Casalbone, D., Sposato, A., Martorelli, E., Alonso, B., & Ercilla, G. (2013). Bathy-morphological setting of Terceira Island (Azores) after the FAIVI cruise. *Journal of Maps*, 9(4), 590–595. <https://doi.org/10.1080/17445647.2013.831381>
- Civello, S., & Margheriti, L. (2004). Toroidal mantle flow around the Calabrian slab (Italy) from SKS splitting. *Geophysical Research Letters*, 31, L10601. <https://doi.org/10.1029/2004GL019607>
- Clague, D. A., Moore, J. G., & Reynolds, J. R. (2000). Formation of submarine flat-topped volcanic cones in Hawai'i. *Bulletin of Volcanology*, 62(3), 214–233. <https://doi.org/10.1007/s004450000088>
- Cocchi, L., Passaro, S., Tontini, F. C., & Ventura, G. (2017). Volcanism in slab tear faults is larger than in island-arcs and back-arcs. *Nature Communications*, 8(1), 1451. <https://doi.org/10.1038/s41467-017-01626-w>
- Coltelli, M., Cavallaro, D., D'Anna, G., D'Alessandro, A., Grassa, F., Mangano, G., & Gresta, S. (2016). Exploring the submarine Graham Bank in the Sicily Channel. *Annals of Geophysics*.
- Cuffaro, M., Martorelli, E., Bosman, A., Conti, A., Bigi, S., Muccini, F., & Scrocca, D. (2016). The Ventotene Volcanic Ridge: A newly explored complex in the central Tyrrhenian Sea (Italy). *Bulletin of Volcanology*, 78(12), 86. <https://doi.org/10.1007/s00445-016-1081-9>
- Damuth, J. E. (1980). Use of high-frequency (3.5–12 kHz) echograms in the study of near-bottom sedimentation processes in the deep-sea: a review. *Marine Geology*, 38(1–3), 51–75. [https://doi.org/10.1016/0025-3227\(80\)90051-1](https://doi.org/10.1016/0025-3227(80)90051-1)
- Dannowski, A., Morgan, J. P., Grevemeyer, I., & Ranero, C. R. (2018). Enhanced mantle upwelling/melting caused segment propagation, oceanic core complex die off, and the death of a transform fault: The mid-Atlantic ridge at 21.5°N. *Journal of Geophysical Research: Solid Earth*, 123, 941–956. <https://doi.org/10.1002/2017JB014273>
- De Astis, G., Ventura, G., & Vilardo, G. (2003). Geodynamic significance of the Aeolian volcanism (Southern Tyrrhenian Sea, Italy) in light of structural, seismological, and geochemical data. *Tectonics*, 22(4), 1040. <https://doi.org/10.1029/2003TC001506>
- De Ritis, R., Dominici, R., Ventura, G., Nicolosi, I., Chiappini, M., Speranza, F., & Sonnino, M. (2010). A buried volcano in the Calabrian Arc (Italy) revealed by high-resolution aeromagnetic data. *Journal of Geophysical Research*, 115, B11101. <https://doi.org/10.1029/2009JB007171>
- de Voogd, B., Truffert, C., Chamot-Rooke, N., Huchon, P., Lallemand, S., & Le Pichon, X. (1992). Two-ship deep seismic soundings in the basins of the Eastern Mediterranean Sea (Pasiphae cruise). *Geophysical Journal International*, 109(3), 536–552. <https://doi.org/10.1111/j.1365-246X.1992.tb00116.x>
- Dellong, D., Klingelhoefer, F., Kopp, H., Graindorge, D., & Margheriti, L. (2018). Crustal structure of the Ionian basin and eastern Sicily margin: Results from a wide-angle seismic survey. *Journal of Geophysical Research: Solid Earth*, 123, 2090–2114. <https://doi.org/10.1002/2017JB015312>
- Faccenna, C., Becker, T. W., Lallemand, S., Lagabrielle, Y., Funicello, F., & Piromallo, C. (2010). Subduction-triggered magmatic pulses: A new class of plumes? *Earth and Planetary Science Letters*, 299(1–2), 54–68. <https://doi.org/10.1016/j.epsl.2010.08.012>
- Faccenna, C., Becker, T. W., Lucente, F. P., Jolivet, L., & Rossetti, F. (2001). History of subduction and back arc extension in the Central Mediterranean. *Geophysical Journal International*, 145(3), 809–820. <https://doi.org/10.1046/j.0956-540x.2001.01435.x>
- Faccenna, C., Civetta, L., Antonio, M. D., Funicello, F., Margheriti, L., & Piromallo, C. (2005). Constraints on mantle circulation around the deforming Calabrian slab. *Geophysical Research Letters*, 32, L06311. <https://doi.org/10.1029/2004GL021874>
- Faccenna, C., Funicello, F., Piromallo, C., Rossetti, F., Giardini, D., & Funicello, R. (2004). Subduction and back-arc extension in the Tyrrhenian Sea. *Memorie Descrittive Carta Geologica d' Italia*, XLIV, 165–184.
- Faccenna, C., Molin, P., Orecchio, B., Olivetti, V., Bellier, O., Funicello, F., & Billi, A. (2011). Topography of the Calabria subduction zone (southern Italy): Clues for the origin of Mt. Etna. *Tectonics*, 30, TC1003. <https://doi.org/10.1029/2010TC002694>
- Ferranti, L., Burrato, P., Pepe, F., Santoro, E., Mazzella, M. E., Morelli, D., & Vannucci, G. (2014). An active oblique-contractional belt at the transition between the Southern Apennines and Calabrian Arc: The Amendolara Ridge, Ionian Sea, Italy. *Tectonics*, 33, 2169–2194. <https://doi.org/10.1002/2014TC003624>
- Ferrari, L., & Manetti, P. (1993). Geodynamic framework of the Tyrrhenian volcanism: A review. *Acta Vulcanol*, 3, 1–10.
- Finetti, I., & Del Ben, A. (1986). Geophysical study of the Tyrrhenian opening. *Bollettino Di Geofisica Teorica e Applicata*, 28, 75–155.
- Finetti, I. R. (2005). *CROP project: Deep seismic exploration of the central Mediterranean and Italy* (Vol. 1). Elsevier.
- Foulger, G. R., Panza, G. F., Artemieva, I. M., Bastow, I. D., Cammarano, F., Evans, J. R., & Thybo, H. (2013). Caveats on tomographic images. *Terra Nova*, 25(4), 259–281. <https://doi.org/10.1111/ter.12041>
- Funicello, F., Moroni, M., Piromallo, C., Faccenna, C., Cenedese, A., & Bui, H. A. (2006). Mapping mantle flow during retreating subduction: Laboratory models analyzed by feature tracking. *Journal of Geophysical Research*, 111, B03402. <https://doi.org/10.1029/2005JB003792>
- Gasparon, M., Rosenbaum, G., Wijbrans, J., & Manetti, P. (2009). The transition from subduction arc to slab tearing: Evidence from Capraia Island, northern Tyrrhenian Sea. *Journal of Geodynamics*, 47(1), 30–38. <https://doi.org/10.1016/j.jog.2008.06.004>
- Gillot, P. Y. (1987). Histoire volcanique des Iles Eoliennes: Arc insulaire ou complexe orogénique anulaire. *Doc Trav IGAL*, 11, 35–42.
- Goes, S., Giardini, D., Jenny, S., Hollenstein, C., Kahle, H., & Geiger, A. (2004). A recent tectonic reorganization in the south-central Mediterranean. *Earth and Planetary Science Letters*, 226(3–4), 335–345. <https://doi.org/10.1016/j.epsl.2004.07.038>
- González, P. J., Samsonov, S. V., Pepe, F., Tiampo, K. F., Tizzani, P., Casu, F., & Sansosti, E. (2013). Magma storage and migration associated with the 2011–2012 El Hierro eruption: Implications for crustal magmatic systems at oceanic island volcanoes. *Journal of Geophysical Research: Solid Earth*, 118, 4361–4377. <https://doi.org/10.1002/jgrb.50289>
- Govers, R., & Wortel, M. J. R. (2005). Lithosphere tearing at STEP faults: Response to edges of subduction zones. *Earth and Planetary Science Letters*, 236(1–2), 505–523. <https://doi.org/10.1016/j.epsl.2005.03.022>
- Gueguen, E., Doglioni, C., & Fernandez, M. (1998). On the post-25 Ma geodynamic evolution of the western Mediterranean. *Tectonophysics*, 298(1–3), 259–269. [https://doi.org/10.1016/S0040-1951\(98\)00189-9](https://doi.org/10.1016/S0040-1951(98)00189-9)

- Hernández-Molina, F. J., Fernández-Salas, L. M., Lobo, F., Somoza, L., Díaz-del-Río, V., & Dias, J. M. A. (2000). The infralittoral prograding wedge: A new large-scale progradational sedimentary body in shallow marine environments. *Geo-Marine Letters*, *20*(2), 109–117. <https://doi.org/10.1007/s003670000040>
- Ingrassia, M., Martorelli, E., Bosman, A., Macelloni, L., Sposato, A., & Chiocci, F. L. (2015). The Zannone Giant Pockmark: First evidence of a giant complex seeping structure in shallow-water, central Mediterranean Sea, Italy. *Marine Geology*, *363*, 38–51. <https://doi.org/10.1016/j.margeo.2015.02.005>
- Ishizuka, O., Geshi, N., Itoh, J., Kawanabe, Y., & TuZino, T. (2008). The magmatic plumbing of the submarine Hachijo NW volcanic chain, Hachijojima, Japan: Long-distance magma transport? *Journal of Geophysical Research*, *113*, B08S08. <https://doi.org/10.1029/2007JB005325>
- Ismail-Zadeh, A. T., Nicolich, R., & Cernobori, L. (1998). Modelling of geodynamic evolution of the Ionian Sea basin. *Computational Seismology and Geodynamics*, *30*, 32–50.
- Kastens, K., Mascle, J., Aurox, C., Bonatti, E., Broglia, C., Channell, J., & Hasegawa, S. (1988). ODP Leg 107 in the Tyrrhenian Sea: Insights into passive margin and back-arc basin evolution. *Geological Society of America Bulletin*, *100*(7), 1140–1156. [https://doi.org/10.1130/0016-7606\(1988\)100<1140:OLITTS>2.3.CO;2](https://doi.org/10.1130/0016-7606(1988)100<1140:OLITTS>2.3.CO;2)
- Király, Á., Capitanio, F. A., Funicello, F., & Faccenna, C. (2017). Subduction induced mantle flow: Length-scales and orientation of the toroidal cell. *Earth and Planetary Science Letters*, *479*, 284–297. <https://doi.org/10.1016/j.epsl.2017.09.017>
- Kokelaar, B. P., & Durant, G. P. (1983). The submarine eruption and erosion of Surtla (Surtsey), Iceland. *Journal of Volcanology and Geothermal Research*, *19*(3–4), 239–246. [https://doi.org/10.1016/0377-0273\(83\)90112-9](https://doi.org/10.1016/0377-0273(83)90112-9)
- Koulakov, I. (2009). LOTOS code for local earthquake tomographic inversion: Benchmarks for testing tomographic algorithms. *Bulletin of the Seismological Society of America*, *99*(1), 194–214. <https://doi.org/10.1785/0120080013>
- Lallemant, S., Font, Y., Bijwaard, H., & Kao, H. (2001). New insights on 3-D plates interaction near Taiwan from tomography and tectonic implications. *Tectonophysics*, *335*(3–4), 229–253. [https://doi.org/10.1016/S0040-1951\(01\)00071-3](https://doi.org/10.1016/S0040-1951(01)00071-3)
- Leahy, G. M., & Bercovici, D. (2007). On the dynamics of a hydrous melt layer above the transition zone. *Journal of Geophysical Research*, *112*, B07401. <https://doi.org/10.1029/2006JB004631>
- Lawrence, R. L., Means, J. E., Ripple, W. J. (1996). An automated method for digitizing color thematic maps. *Photogrammetric Engineering and Remote Sensing*, *62*, 1245–1248.
- Levin, V., Shapiro, N., Park, J., & Ritzwoller, M. (2002). Seismic evidence for catastrophic slab loss beneath Kamchatka. *Nature*, *418*(6899), 763–767. <https://doi.org/10.1038/nature00973>
- Li, Y., & Oldenburg, D. W. (2003). Fast inversion of large-scale magnetic data using wavelet transforms and a logarithmic barrier method. *Geophysical Journal International*, *152*(2), 251–265.
- Liu, L., & Stegman, D. R. (2012). Origin of Columbia River flood basalt controlled by propagating rupture of the Farallon slab. *Nature*, *482*(7385), 386–389. <https://doi.org/10.1038/nature10749>
- Locardi, E. (1993). Dynamics of deep structures in the Tyrrhenian-Apennines area and its relation to neotectonics. *Il Quaternario*, *6*, 59–66.
- Locardi, E., & Nicolich, R. (2005). Crust-mantle structures and Neogene-quaternary magmatism in Italy. *Bollettino Di Geofisica Teorica Ed Applicata*, *46*(2–3), 169–180.
- Loreto, M. F., Pepe, F., De Ritis, R., Ventura, G., Ferrante, V., Speranza, F., & Sacchi, M. (2015). Geophysical investigation of Pleistocene volcanism and tectonics offshore Capo Vaticano (Calabria, southeastern Tyrrhenian Sea). *Journal of Geodynamics*, *90*, 71–86. <https://doi.org/10.1016/j.jog.2015.07.005>
- Lucente, F. P., Chiarabba, C., Cimini, G. B., & Giardini, D. (1999). Tomographic constraints on the geodynamic evolution of the Italian region. *Journal of Geophysical Research*, *104*(B9), 20,307–20,327. <https://doi.org/10.1029/1999JB900147>
- Lustrino, M., & Wilson, M. (2007). The circum-Mediterranean anorogenic Cenozoic igneous province. *Earth-Science Reviews*, *81*(1–2), 1–65. <https://doi.org/10.1016/j.earscirev.2006.09.002>
- Malinverno, A., Cafiero, M., Ryan, W. B. F., & Cita, M. B. (1981). Distribution of messinian sediments and erosional surfaces beneath the tyrrhenian sea-geodynamic implications. *Oceanologica Acta*, *4*(4), 489–495.
- Marani, M. P., & Trua, T. (2002). Thermal constriction and slab tearing at the origin of a superinflated spreading ridge: Marsili volcano (Tyrrhenian Sea). *Journal of Geophysical Research*, *107*(B9), 2188. <https://doi.org/10.1029/2001JB000285>
- Martorelli, E., Italiano, F., Ingrassia, M., Macelloni, L., Bosman, A., Conte, A. M., & Chiocci, F. L. (2016). Evidence of a shallow water submarine hydrothermal field off Zannone Island from morphological and geochemical characterization: Implications for Tyrrhenian Sea Quaternary volcanism. *Journal of Geophysical Research: Solid Earth*, *121*, 8396–8414. <https://doi.org/10.1002/2016JB013103>
- Milia, A., Turco, E., Pierantoni, P. P., & Schettino, A. (2009). Four-dimensional tectono-stratigraphic evolution of the Southeastern peri-Tyrrhenian basins (Margin of Calabria, Italy). *Tectonophysics*, *476*(1–2), 41–56. <https://doi.org/10.1016/j.tecto.2009.02.030>
- Miller, M. S., Gorbatov, A., & Kennett, B. L. N. (2006). Three-dimensional visualization of a near-vertical slab tear beneath the southern Mariana arc. *Geochemistry, Geophysics, Geosystems*, *7*, Q06012. <https://doi.org/10.1029/2005GC001110>
- Mitchell, N. C., Masselink, G., Huthnance, J. M., Fernández-Salas, L. M., & Lobo, F. J. (2012). Depths of modern coastal sand cliniforms. *Journal of Sedimentary Research*, *82*(7), 469–481. <https://doi.org/10.2110/jsr.2012.40>
- Montuori, C., Cimini, G. B., & Favali, P. (2007). Teleseismic tomography of the southern Tyrrhenian subduction zone: New results from seafloor and land recordings. *Journal of Geophysical Research*, *112*, B03311. <https://doi.org/10.1029/2005JB004114>
- Neri, G., Marotta, A. M., Orecchio, B., Presti, D., Totaro, C., Barzaghi, R., & Borghi, A. (2012). How lithospheric subduction changes along the Calabrian Arc in southern Italy: geophysical evidences. *International Journal of Earth Sciences*, *101*(7), 1949–1969. <https://doi.org/10.1007/s00531-012-0762-7>
- Neri, G., Orecchio, B., Totaro, C., Falcone, G., & Presti, D. (2009). Subduction beneath southern Italy close the ending: Results from seismic tomography. *Seismological Research Letters*, *80*(1), 63–70. <https://doi.org/10.1785/gssrl.80.1.63>
- Nicolosi, I., Speranza, F., & Chiappini, M. (2006). Ultrafast oceanic spreading of the Marsili Basin, southern Tyrrhenian Sea: Evidence from magnetic anomaly analysis. *Geology*, *34*(9), 717–720. <https://doi.org/10.1130/G22555.1>
- Nijholt, N., & Govers, R. (2015). The role of passive margins on the evolution of Subduction-Transform Edge Propagators (STEPS). *Journal of Geophysical Research: Solid Earth*, *120*, 7203–7230. <https://doi.org/10.1002/2015JB012202>
- Nolet, G. (1987). *Seismic wave propagation and seismic tomography*. In *Seismic tomography* (pp. 1–23). Springer.
- Orecchio, B., Presti, D., Totaro, C., Guerra, I., & Neri, G. (2011). Imaging the velocity structure of the Calabrian Arc region (southern Italy) through the integration of different seismological data. *Bollettino Di Geofisica Teorica Ed Applicata*, *52*(4).
- Orecchio, B., Presti, D., Totaro, C., & Neri, G. (2014). What earthquakes say concerning residual subduction and STEP dynamics in the Calabrian Arc region, south Italy. *Geophysical Journal International*, *199*(3), 1929–1942. <https://doi.org/10.1093/gji/ggu373>



- Paige, C. C., & Saunders, M. A. (1982). LSQR: An algorithm for sparse linear equations and sparse least squares. *ACM Transactions on Mathematical Software (TOMS)*, *8*(1), 43–71. <https://doi.org/10.1145/355984.355989>
- Panza, G. F., Chimera, G., Pontevivo, A., Aoudia, A., & Raykova, R. (2003). The lithosphere-asthenosphere: Italy and surroundings.
- Parson, L. M., Murton, B. J., Searle, R. C., Booth, D., Evans, J., Field, P., & Millard, N. (1993). En echelon axial volcanic ridges at the Reykjanes Ridge: A life cycle of volcanism and tectonics. *Earth and Planetary Science Letters*, *117*(1–2), 73–87. [https://doi.org/10.1016/0012-821X\(93\)90118-S](https://doi.org/10.1016/0012-821X(93)90118-S)
- Passaro, S., Milano, G., D'Isanto, C., Ruggieri, S., Tonielli, R., Bruno, P. P., & Marsella, E. (2010). DTM-based morphometry of the Palinuro seamount (Eastern Tyrrhenian Sea): Geomorphological and volcanological implications. *Geomorphology*, *115*(1–2), 129–140. <https://doi.org/10.1016/j.geomorph.2009.09.041>
- Peccerillo, A. (2017). *Cenozoic volcanism in the Tyrrhenian Sea region*. Springer.
- Pepe, F., Bertotti, G., Ferranti, L., Sacchi, M., Collura, A. M., Passaro, S., & Sulli, A. (2014). Pattern and rate of post-20 ka vertical tectonic motion around the Capo Vaticano Promontory (W Calabria, Italy) based on offshore geomorphological indicators. *Quaternary International*, *332*, 85–98. <https://doi.org/10.1016/j.quaint.2013.11.012>
- Pepe, F., Sulli, A., Bertotti, G., & Cella, F. (2010). Architecture and Neogene to Recent evolution of the western Calabrian continental margin: An upper plate perspective to the Ionian subduction system, central Mediterranean. *Tectonics*, *29*, TC3007. <https://doi.org/10.1029/2009TC002599>
- Piomallo, C., & Morelli, A. (2003). P wave tomography of the mantle under the Alpine-Mediterranean area. *Journal of Geophysical Research*, *108*(B2), 2065. <https://doi.org/10.1029/2002JB001757>
- Prada, M., Ranero, C. R., Sallarès, V., Zitellini, N., & Grevemeyer, I. (2016). Mantle exhumation and sequence of magmatic events in the Magnaghi–Vavilov Basin (Central Tyrrhenian, Italy): New constraints from geological and geophysical observations. *Tectonophysics*, *689*, 133–142. <https://doi.org/10.1016/j.tecto.2016.01.041>
- Quartau, R., Hipólito, A., Romagnoli, C., Casalbore, D., Madeira, J., Tempera, F., & Chiocci, F. L. (2014). The morphology of insular shelves as a key for understanding the geological evolution of volcanic islands: Insights from Terceira Island (Azores). *Geochemistry, Geophysics, Geosystems*, *15*, 1801–1826. <https://doi.org/10.1002/2014GC005248>
- Reynolds, J. M. (2011). *An introduction to applied and environmental geophysics*. John Wiley & Sons.
- Romagnoli, C., Casalbore, D., Ricchi, A., Lucchi, F., Quartau, R., Bosman, A., & Chiocci, F. L. (2018). Morpho-bathymetric and seismo-stratigraphic analysis of the insular shelf of Salina (Aeolian archipelago) to unveil its Late-Quaternary geological evolution. *Marine Geology*, *395*, 133–151. <https://doi.org/10.1016/j.margeo.2017.10.003>
- Romagnoli, C., & Jakobsson, S. P. (2015). Post-eruptive morphological evolution of island volcanoes: Surtsey as a modern case study. *Geomorphology*, *250*, 384–396. <https://doi.org/10.1016/j.geomorph.2015.09.016>
- Rosenbaum, G., Gasparon, M., Lucente, F. P., Peccerillo, A., & Miller, M. S. (2008). Kinematics of slab tear faults during subduction segmentation and implications for Italian magmatism. *Tectonics*, *27*, TC2008. <https://doi.org/10.1029/2007TC002143>
- Sacks, P. E., & Secor, D. T. Jr. (1990). Delamination in collisional orogens. *Geology*, *18*(10), 999–1002. [https://doi.org/10.1130/0091-7613\(1990\)018<0999:DICO>2.3.CO;2](https://doi.org/10.1130/0091-7613(1990)018<0999:DICO>2.3.CO;2)
- Santo, A. P., & Clark, A. H. (1994). Volcanological evolution of Aeolian Arc, Italy: Inferences from 40Ar/39Ar ages of Filicudi rocks. IAVCEI Congress, Abstract Volume, Ankara, 1994.
- Savelli, C. (2000). Two-stage progression of volcanism 8–0 Ma in the central Mediterranean southern Italy. *Journal of Geodynamics*, *31*, 87–104.
- Sartori, R., Torelli, L., Zitellini, N., Carrara, G., Magaldi, M., & Mussoni, P. (2004). Crustal features along a W-E Tyrrhenian transect from Sardinia to Campania margins (Central Mediterranean). *Tectonophysics*, *383*(3–4), 171–192. <https://doi.org/10.1016/j.tecto.2004.02.008>
- Savelli, C. (2015). Fast Episodes of West-Mediterranean-Tyrrhenian oceanic opening and revisited relations with tectonic setting. *Scientific Reports*, *5*, 14,271.
- Savelli, C. (1988). Late Oligocene to Recent episodes of magmatism in and around the Tyrrhenian Sea: Implications for the processes of opening in a young inter-arc basin of intra-orogenic (Mediterranean) type. *Tectonophysics*, *146*(1–4), 163–181. [https://doi.org/10.1016/0040-1951\(88\)90089-3](https://doi.org/10.1016/0040-1951(88)90089-3)
- Scarfì, L., & Barberi, G. (2018). Slab narrowing in the Central Mediterranean: The Calabro-Ionian subduction zone as imaged by high resolution seismic tomography. *Scientific Reports*, *8*(1), 5178. <https://doi.org/10.1038/s41598-018-23543-8>
- Schwartz, D. M., Soule, S. A., Wanless, V. D., & Jones, M. R. (2018). Identification of erosional terraces on seamounts: Implications for interisland connectivity and subsidence in the Galápagos Archipelago. *Frontiers in Earth Science*, *6*, 88. <https://doi.org/10.3389/feart.2018.00088>
- Scrocca, D., Doglioni, C., Innocenti, F., Manetti, P., Mazzotti, A., Bertelli, L., D'Offizi, S. (2003). CROP ATLAS-Seismic Reflection Profiles of the Italian Crust (Vol. 62).
- Sedimentari, B. (1980). Dati geologici preliminari sul bacino di Cefalu (Mar Tirreno). *Ateneo Parmense Acta Nat*, *16*, 3–18.
- Smith, D. K., & Cann, J. R. (1999). Constructing the upper crust of the Mid-Atlantic Ridge: A reinterpretation based on the Puna Ridge, Kilauea Volcano. *Journal of Geophysical Research*, *104*(B11), 25,379–25,399. <https://doi.org/10.1029/1999JB900177>
- Strak, V., & Schellart, W. P. (2014). Evolution of 3-D subduction-induced mantle flow around lateral slab edges in analogue models of free subduction analysed by stereoscopic particle image velocimetry technique. *Earth and Planetary Science Letters*, *403*, 368–379. <https://doi.org/10.1016/j.epsl.2014.07.007>
- Tempera, F., Hipólito, A., Madeira, J., Vieira, S., Campos, A. S., & Mitchell, N. C. (2013). Condor seamount (Azores, NE Atlantic): A morpho-tectonic interpretation. *Deep Sea Research Part II: Topical Studies in Oceanography*, *98*, 7–23. <https://doi.org/10.1016/j.dsr2.2013.09.016>
- Tibaldi, A. (2015). Structure of volcano plumbing systems: A review of multi-parametric effects. *Journal of Volcanology and Geothermal Research*, *298*, 85–135. <https://doi.org/10.1016/j.jvolgeores.2015.03.023>
- Totaro, C., Koulakov, I., Orecchio, B., & Presti, D. (2014). Detailed crustal structure in the area of the southern Apennines–Calabrian Arc border from local earthquake tomography. *Journal of Geodynamics*, *82*, 87–97. <https://doi.org/10.1016/j.jog.2014.07.004>
- Totaro, C., Seeber, L., Waldhauser, F., Steckler, M., Gervasi, A., Guerra, I., & Presti, D. (2015). An intense earthquake swarm in the southernmost Apennines: Fault architecture from high-resolution hypocenters and focal mechanisms intense earthquake swarm in the southernmost Apennines. *Bulletin of the Seismological Society of America*, *105*(6), 3121–3128. <https://doi.org/10.1785/0120150074>
- Trua, T., Serri, G., Marani, M. P., Marina, G., Gobetti, V., & Bologna, I. (2003). Lateral flow of African mantle below the nearby Tyrrhenian plate: Geochemical evidence. *Terra Nova*, *15*(6), 433–440. <https://doi.org/10.1046/j.1365-3121.2003.00509.x>
- Trua, T., Serri, G., Marani, M. P., Rossi, P. L., Gamberi, F., & Renzulli, A. (2004). Mantle domains beneath the southern Tyrrhenian: Constraints from recent seafloor sampling and dynamic implications. *Periodico Di Mineralogia*, *73*, 53–73.
- Vacquier, V. (1972). *Geomagnetism in marine geology*, (Vol. 6). Elsevier.

- Westaway, R., Oldenburg, D. W. (1993). Quaternary uplift of southern Italy. *Journal of Geophysical Research*, 98(B12), 21,741–21,772.
- Wortel, M. J. R., & Spakman, W. (2000). Subduction and slab detachment in the Mediterranean-Carpathian region. *Science*, 290(5498), 1910–1917. <https://doi.org/10.1126/science.290.5498.1910>
- Würtz, M., & Rovere, M. (2015). Atlas of the Mediterranean seamounts and seamount-like structures. IUCN.